FAKULTA
STAVEBNÍ
ČVUT V PRAZE

Soutěž o cenu akademika Bažanta

Akademický rok 2024/2025

Thermal Crack Mitigation in Massive Concrete Structures with Cooling Pipes

Milan Macho

Praha, Duben 2025

Autor práce:
Milan Macho
2. navazující ročník, obor K
Fakulta stavební
České vysoké učení technické v Praze
Thákurova 7
166 29 Praha 6
Česká republika
milan.macho@fsv.cvut.cz

Vedoucí práce:
prof. Ing. Vít Šmilauer, Ph.D., DSc.
Katedra mechaniky K132
Fakulta stavební
České vysoké učení technické v Praze
Thákurova 7
166 29 Praha 6
Česká republika
vit.smilauer@cvut.cz

Abstract

This work investigates the thermal and mechanical behaviour of a concrete pilot block, which forms part of a flood prevention polder on the Krounka River in the Czech Republic. Particular attention is paid to the early-age behaviour of the structure and the development of cracks as a result of hydration heat. A numerical model is developed using the object-oriented finite element software OOFEM, supported by open-source tools for pre- and post-processing. Cement hydration is simulated using the affinity hydration model, with parameters calibrated from experimental data. Thermal analysis is formulated as a transient heat transfer problem and validated using temperature data from embedded sensors.

The nonlinear mechanical analysis is coupled with the thermal simulation results. Concrete is modelled as an ageing viscoelastic material with tensile fracture behaviour. Basic creep and autogenous shrinkage are described by the Microprestress–Solidification theory, and fracture behaviour is captured using a fixed crack model. Model parameters are derived primarily from experiments, supplemented by literature values where necessary. The mechanical analysis results are compared with in situ strain data, overall showing good agreement. The evolution of the crack width is also the key objective.

The findings indicate that the structure is not prone to early-age cracking under realistic boundary conditions. However, it is highly sensitive to restraint. When base concrete is modelled as fully rigid, significant through-cracks can occur. The study highlights the importance of embedded cooling systems in reducing thermal stresses and demonstrates the applicability of numerical modelling as an effective tool for the design and evaluation of cracking risk for massive concrete structures.

Keywords

Massive concrete, Thermal cracking, Pipe cooling system, Polder, Finite element method (FEM), OOFEM, Thermal analysis, Mechanical analysis, Hydration heat, Creep, Shrinkage, Fracture, Affinity model, Microprestress-solidification, Monitoring

Acknowledgement

I would like to express my sincere gratitude to all those who helped and supported me during the work on these pages. Special thanks go to my supervisor, prof. Ing. Vít Šmilauer, Ph.D., DSc. , for his valuable advice, patience and expert guidance. His support and encouragement were essential to the completion of this work.

Contents

Chapter 1

Introduction

1.1 Background

Reinforced concrete is one of the most widely used civil engineering materials due to its high compressive strength, excellent workability, cost-efficiency, and durability. However, its durability can be compromised by the propagation and development of cracks. These cracks can arise from various causes, including structural issues such as overloading or unexpected settlements, as well as non-structural factors like shrinkage, creep, and thermal actions. This second type of cracks can be partly mitigated through proper design, disciplined construction practices, and effective curing. Still, the issue remains very complex and challenging. When speaking about the thermal actions, the released hydration heat, combined with low thermal conductivity, results in high temperature gradients in massive concrete structures, causing problems that have to be considered in the design. An effective technique for dissipating heat during curing is water cooling of the core part using pre-installed pipe lining.

One of the most remarkable examples, where civil engineers have to face this challenge, is during the construction of the dams. The most remarkable examples are large dams such as Hoover Dam (USA, 1936), Itaipu Dam (Brazil/Paraguy, 1984), Kariba Dam (Zambia/Zimbabwe, 1960) or Three Gorges Dam (China, 2003). Despite the different location, type or age, all the above-mentioned dams have one thing in common that special interest had to be given to the released hydration heat and the technique of water-cooling pipe lining had been employed. Left unchecked, hydration heat could cause significant thermal cracking, compromising not only the dam's structural integrity but also leading to water seepage and finally increasing maintenance and repair costs. Reducing the risk of cracking and understanding its underlying mechanisms remain key objectives for researchers. Despite significant progress over the past century, some questions remain unanswered and new ones continue to emerge. This reflects the complexity and interdisciplinary nature of the field. For many scientists, this field becomes a lifelong pursuit.

In my case, the master's thesis represents a natural progression in this area of study. My initial introduction to the topic was during the bachelor thesis, which as well focused on modelling the water-cooling process in massive concrete structures and exploring cement hydration [20]. That work focused on the comparison of heat field evolution for simplified and detailed geometry including cooling pipes. This experience has provided a strong foundation and also a passion for further research.

1.2 Aim and scope

The behaviour of massive water-cooled concrete structures is influenced by complex thermo-mechanical interactions, particularly under conditions of restrained shrinkage, creep and cooling-induced stresses. While extensive empirical data and established models exist for conventional restrained concrete, the specific characteristics of large-scale, water-cooled concrete constructions remain insufficiently explored in terms of predictive accuracy. Possible reasons for an explanation why so, probably come from the difficulty of generalization. Each large-scale structure is quite unique because of its geometry, concrete mixture recipe, restraint conditions, curing technique, boundary conditions, surrounding temperature and so on. It is quite obvious that it can be hardly generalized and, therefore, a numerical analysis is a necessity for such structures.

This thesis's hypothesis is that coupled thermo-mechanical simulations can accurately predict stress evolution, cracking behaviour, and deformation in water-cooled concrete blocks, if material parameters and boundary conditions are appropriately assumed. Therefore, finite element software is utilized in order to replicate the heat development caused by hydration and simulate the propagation and development of cracks in the block of a dam structure. The key research questions are divided into three main areas:

- **Material Modelling:** How effectively can existing mechanical models combined with the fracture model simulate crack propagation in massive water-cooled concrete structures under real-world conditions?
- **Validation Framework:** How effectively can in situ measurements, such as data from instrumented blocks, validate the numerical simulations?

In addition, the thesis intends to investigate the potential applicability of these results to other possible applications.

Numerical modelling requires careful selection of factors to include, balancing accuracy with computational complexity. Background variables, such as the insulation of formwork or the top surface covering, are relatively straightforward to consider. However, others are more difficult. The air temperature, which can vary significantly from day to night, generates a dynamic boundary condition that is more difficult to parametrise. These temperature changes can further produce thermal gradients that might affect hydration and stress development. Also, the long duration of casting makes modelling more challenging because the initial temperature of fresh concrete is different for each batch, leading to nonuniform hydration of the block. While these effects would greatly enhance the fidelity of the model, they significantly complicate it. Simplifications, such as assuming average temperatures or uniform hydration, are practical for reducing computational requirements. However, their potential impact on results, particularly for stress distribution and cracking risk, should be carefully evaluated to ensure the model remains relevant to real-world conditions.

1.3 Outline

Second chapter "State of the Art" underlines the importance of this problem and provides the reasoning for importance of this topic. The fundamental object of this chapter is to provide an explanation of the mechanism for the cracking of massive concrete structures in the early stage and present the types of possible cracks. Furthermore, it describes adopted possible ways how to mitigate this risk as well as the overview of modelling approaches and comparison between adoption of the embedded pipe water-cooling in Sweden and Czechia.

The central part of the work consists of chapter 3 "Finite Element Analysis" and chapter 4 "Polder Krounka". Third chapter focuses on the finite element analysis, in which crack development in a massive water-cooled concrete block is the main interest. The numerical model employs a multi-physical approach. Important part of this chapter is the review of the models describing time-dependent phenomenons for concrete such as hydration, viscoelasticity, shrinkage, creep and fracture. The fourth chapter presents an objective of the thesis which is a part of the upstream wall of a dam preventing floods on the river Krounka in the Pardubice Region, the Czech Republic. It describes data obtained from in situ measurements and laboratory data, which provide a solid basis for model validation. Moreover, a detailed description of the finite element analysis for the structure is described.

In the following fifth chapter, the results of the FE analysis are presented and described. Moreover, the results are also compared with the conducted field experiment. This ensures the validation format for the numerical model. Parameter study compares the impact of different parameter settings and revealing the most important factors. Final chapter "Discussion and Conclusion" summarizes the major findings of this thesis and also puts interest in the possible future research in this area.

Chapter 2

State of the Art

Understanding the nature of mechanical and thermal stresses experienced by concrete structures during curing is a necessary prerequisite for the description of cracking of concrete structures. Thus, it is essential for ensuring the structural capacity, durability, and long life-span of these structures. In other words, proper design reduces maintenance costs and total lifetime costs. This becomes even more important for key infrastructure constructions such as dams, power plants, bridges, containments, harbour structures, etc. The above mentioned structures are very often giant and made of large amount of concrete. Therefore, these structures are usually classified as massive concrete structures.

The apposite description of massive concrete structures provides the American Concrete Institute (ACI): "Any volume of concrete with dimensions large enough to require that measures be taken to cope with the generation of heat from the hydration of the cement and attendant volume change, to minimize cracking [2]." This definition can seem slightly ambiguous, when compared to the definition of Japanese Concrete Institute (JCI). According to JCI, mass concrete structures can be defined as reinforced concrete walls with a thickness greater than 0.5 m restrained at the base or slab structures with thickness at least 0.8 m [17]. However, the JCI also admits that the guidelines are suitable for structures with a high cement content that undergoes a large temperature difference due to hydration. In conclusion, both definitions mention the reason, which is the heat that evolved during the hydration of the cement.

In addition, experiences with the water cooling technique during hydration are a key component to establishing the simplified methods of design. Despite several practical applications in the last 15 years, this technique is still rarely used in Czech construction practice. Fortunately, Sweden has more experience in this field, which led to the establishment of semi-empirical methods. Thus, it provides valuable information about the benefits and limitations of this technique, as well as potential challenges in its broader adoption.

2.1 Cracking

The reason for cracking in the early stage of the concrete maturing is always almost the same. Cracks start to form when the actual tensile stress attains the current tensile strength of the concrete. During the stage of hydration, concrete explores changes from the liquid to the solid state. Therefore, the mechanical behaviour and description of early age properties such as strength, Young's modulus, viscoelastic properties, and fracture energy are essential. However, it is only one part of the problem. The second part should give an explanation for the cause of experienced tensile stresses. The actual cause of cracking is very likely a combination of the correspondings effects:

- shrinkage, creep, hydration heat, alkali aggregate reaction
- restrain conditions, settlements, loads, environment

The first bullet corresponds to the effects which can be partly mitigated with proper design of the concrete mixture while the second bullet corresponds to the background variables that can vary significantly. The aim of this is to illustrate the wide variety of causes. The total experienced strain $\varepsilon_{\mathrm{c}}(t)$ according to the *fib* Model Code 2010 [15], is represented as the sum:

$$\varepsilon_{\mathrm{c}}(t) = \varepsilon_{\mathrm{ci}}(t_0) + \varepsilon_{\mathrm{cc}}(t) + \varepsilon_{\mathrm{cs}}(t) + \varepsilon_{\mathrm{cT}}(t) \tag{2.1}$$

where:

$\varepsilon_{\mathrm{ci}}(t_0)$	is the initial strain at loading,
$\varepsilon_{\mathrm{cc}}(t)$	is the creep strain at time $t > t_0$,
$\varepsilon_{\mathrm{cs}}(t)$	is the shrinkage strain,
$\varepsilon_{\mathrm{cT}}(t)$	is the thermal strain.

In addition, causes such as insufficient design or improper transport and construction measures have a severe consequence in increasing the risk of cracking.

2.1.1 Thermal induced cracks

Firstly, it is important to mention that for structures without external constraints or statically determinate structures with linear temperature profile, no stress will occur. However, the structures will deform. It can be distinguished between two types of thermal stress:

- self-stress - caused by restrained of the structure itself
- restraint stress - caused by boundary restrained conditions of the structure

The heat developed during the intense exothermic hydration of cement is disipated into the surrounding environment. Due to the low thermal conductivity of concrete a significant difference between the temperature of the core part and the temperature of the surface is reached. Consequently, the cross section is loaded with the temperature, resulting in compression in the core and tension on the surface caused by the effect of restricted expansion of the core by the surface part. Subsequently, cracks occur when the tension reaches the tensile strength of the concrete. Based on the tensile deformation capacity, the maximum difference between temperatures can be determined. It is possible to find the value of 20 °C in literature as well as in ACI or JCI guidelines [2; 17].

The surface cracks mainly form at the beginning of the increase in temperature or during the removal of the formwork when the surface cools quickly. Often these cracks close as the tensile stress on the surface decreases or changes in compression. Thus, these cracks usually do not cause severe problems. However, it can be a problem for thinner construction when there are cracks on both sides or a massive construction with a great temperature gradient. Cracks can grow during the contraction period and result in deeper cracks, or in the case of thinner construction, to through cracks. The through cracks reduces the structural capacity as well as the durability.

During the contraction period, when the temperature of the concrete reaches its peak, the core part tries to shrink. When concrete is restrained, the free movement of cast part is not allowed and can lead to development of deep and through cracks. Typically, a structure is exposed to some type of external restraint coming from the construction restriction such as the connection with sublay concrete or with another part of the structure.

2.1.2 Shrinkage induced cracks

The reduction in the volume of the mixture occurs as a consequence of the phase changes that fresh concrete undergoes. The changes in volume are connected with the lower water volume in the liquid phases compared to its volume in the solid phase. Based on the reason for water loss, it is possible to distinguish between three different types of shrinkage:

- Autogenous shrinkage
- Plastic shrinkage
- Drying shrinkage

In civil engineering practice, autogenous shrinkage is related to a change in volume during hydration under sealed conditions. The first phase is linked with the contraction during the hydration of cement minerals due to complex chemical processes, see "first shrinkage" in the Figure 2.1. This stage occurs before and during the initial setting, followed by the expansion of hydrates (especially C-S-H) until the effect of contraction caused by drying becomes significant. During this phase the autogenous shrinkage is related to the formation of air-filled pores in the cement paste, see "second shrinkage" in the Figure 2.1. [19].

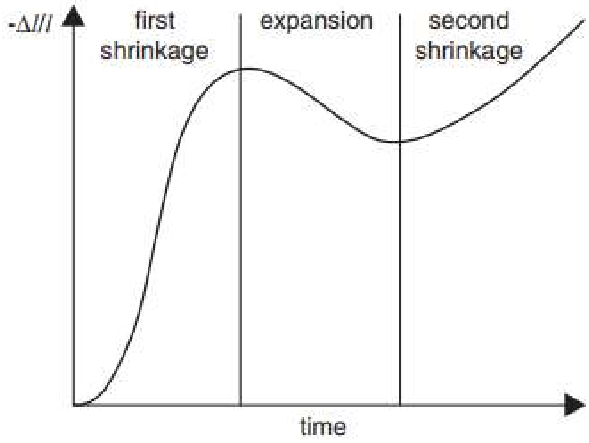

Figure 2.1: Illustration of shrinkage stages of the cement paste [19]

As a product of the chemical reaction, the calcium silicate hydrate mineral (C-S-H) is formed. Based on the molecular mass and densities of the substrates and cement hydration products, volume reduction can be calculated [19]. Thus, chemical shrinkage depends on the mineral composition of the cement. For tricalcium aluminate (C_3A), volume reduction is the highest 7 %, for tricalcium silicate (C_3S) 2.8 %, and for dicalcium silicate (C_2S) is 1 % [19]. During this stage, random cracks can form at the interface of the aggregate and mortar due to unevenly distributed tensile stress [29].

The cast concrete is in the plastic stage during setting until the final setting time. The water from the top surface area rapidly evaporates. This phenomenon is called plastic shrinkage [19]. Rapid moisture evaporation increases internal stress, which can lead to the formation of map cracks on the surface [29]. To minimise the risk of cracking, immediate curing of the concrete surface should be applied. Generally, the main factors affecting plastic shrinkage are capillary pressure, water-cement ratio and the use of admixtures [22].

Drying shrinkage continues to occur when the concrete surface is exposed to environmental conditions which results in the loss of water through the surface. Humidity is distributed non homogenously, introducing strain gradients across the section. The surface dries and attempts to shrink, but it is restrained by the core part. This induces the cracks from the surface. Then the core dries and shrinks. When subjected to restraint, induced tensile stress leads to propagation of the previously formed cracks throughout the section [22].

The decision on which type of shrinkage has the greatest influence depends on the recipe of the concrete mixture. Mixtures with a low water-cement ratio (w/c), finely ground cements, and mixtures containing a high amount of cements, such as high-strength concretes, suffer from high autogenous shrinkage. In this case, the nanopores formed as a result of autogenous shrinkage absorb more water. Moreover, the capillary water content in initial mix is reduced, as well as the diameters of these capillaries are narrower and their tensile stresses are higher. [19]

Blending cement with mineral and pozzolanic materials generally reduces autogenous shrinkage. The effect is that the hydration or pozzolanic reaction of these additions occurs more slowly and hence these particles remain much longer as the anhydrous paste component [19]. Another option is to increase w/c ratio. When the w/c ratio is above 0.5, autogenous shrinkage does not cause any harm due to larger capillaries [19]. However, with increasing w/c ratio, drying shrinkage becomes more dominant as a result of evaporation of free water in the mixture [22]. Furthermore, environmental conditions such as wind speed and sun radiation increase the effect of drying shrinkage.

Most of the concrete shrinkage cracks are surface cracks of fine widths with complex and irregular shapes. Among different types of shrinkage, autogenous shrinkage, plastic shrinkage and drying shrinkage are the main influential factors on the development of shrinkage induced cracks at the early age.

2.1.3 Alkali aggregate reaction

Alkali aggregate reaction (AAR) is related to the chemical interaction between alkali minerals in cement with reactive substances of the aggregate. There are two types of AAR: alkali-carbonate reaction (ACR) and alkali-silica reaction (ASR) [11]. ASR is more frequent and is caused by reactive silica minerals, such as opal, flint, quartz, or volcanic ash. The result of the reaction is the formation of an alkali-silica gel (see Figure b) that expands when exposed to moisture [4]. Therefore, it is a severe problem for constructions such as dams, which are exposed to high moisture.

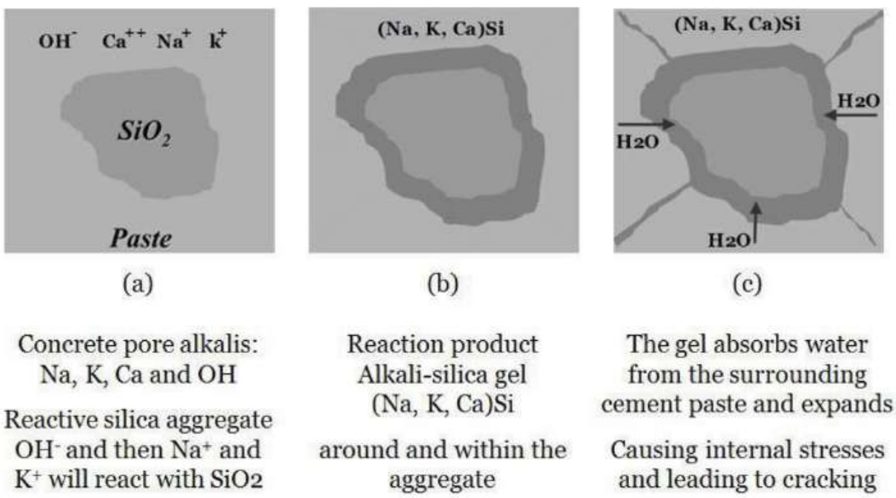

Figure 2.2: Mechanism of alcali-silicate reaction [4]

The micropores are first filled, and then the gel continues to expand, increasing the pressure between the mortar and aggregate. As a result, the mortar around aggregate starts to crack. The cracks develop within the inner part and extend up to the surface. This can form cracks with widths from millimetres up to centimetres. Repair of these cracks is complicated, and the through cracks also lead to the moisture exposure of the reinforcement which can corrode. [29; 4]

The alkali aggregate reaction significantly reduces the tensile and flexural strengths, whereas the effect on the compressive strength is little. In addition, the elastic modulus is significantly reduced due to the formation of cracks. [3]

Figure 2.3: Cracks induced by ASR in the left abutment of the dam Minas Gerais in Brazil. It was constructed in 1946 and the first cracks were observed 20 years after construction. [11]

Cracking caused by AAR is not evident in the early age of concrete due to the cracking mechanism, but the effect on increasing the risk of cracking in the early age is evident due to the lower tensile strength [29]. To reduce the risk of AAR, low-alkali Portland cement, mineral admixtures (fly ash and silica fume) or chemical additives are often used to reduce the expansion. It is clear, that this phenomenon negatively affects the durability of the concrete structures before the end of their proposed life-span.

2.2 Hydration heat

The hydration of cement with water is a complex heterogeneous process with a mechanism not fully described and extensively discussed. It has been studied almost from the beginning of concrete production. Therefore, at the end of the nineteenth century two main theories for cement hydration were introduced.

Le Chatelier established the theory on the basis of the investigation of the hydration of calcium silicates as well as lime. This theory is nowadays known as "crystalloid theory". The proposal that all hydration products are crystalline and responsible for the strength has been the subject of dispute. This led to the formation of "colloid theory" by Wilhelm Michaëlis. His theory assumed, that at first the calcium aluminates and calcium sulphates form the needle crystals around the cement particle. In an environment rich in calcium ions, the hydrosilicate gel forms and embeds the cement particle. The hydration of the cement continues as the particle reacts with the water from the gel. When water cannot penetrate the compact gel, the hydration stops and anhydrous core of the cement particle might remain.

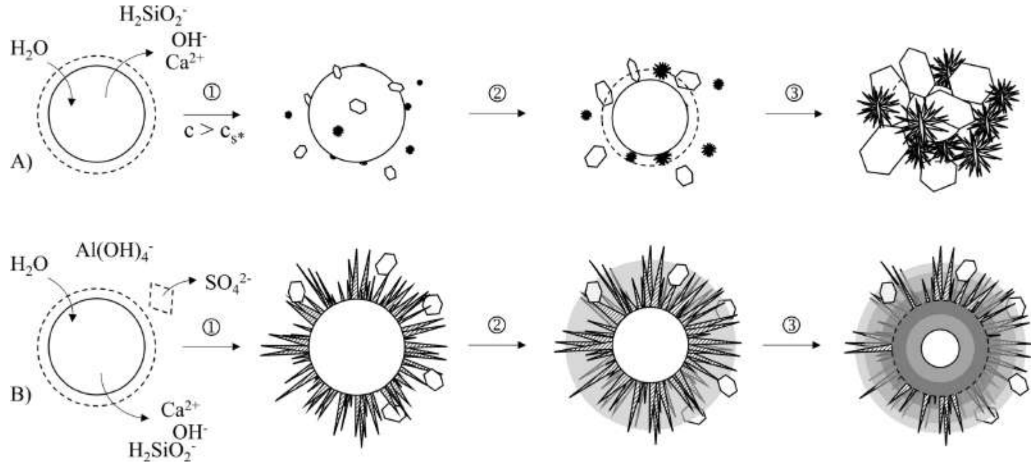

Figure 2.4: Mechanism of cement hydration according to Le Chatelier "crystalloid theory" (A) and Michaëlis "colloid theory" (B)

Kurdowski [19] distinguishes between the heat of hardening and the heat of the hydration. In practice, by heat of hydration we mean the heat that is generated during the hydration of cement minerals and the hardening. In terms of strictness, the heat of hydration should be related only to the chemical reaction when the composition of the final products is exactly known. However, it is useful to determine the amount of heat evolved during hardening for different cement minerals in order to understand the importance of mineral content of cements and their behaviour, see Table 2.1 representing typical values and description of evolution. The mineral composition of the cement strongly influences the evolution and total hydration heat generated by the cement.

Table 2.1: Hydration characteristics of cement minerals [19]

Cement mineral	Hydration heat ($J \cdot g^{-1}$)	Reaction rate
Tricalcium silicate (C_3S)	507	moderate
Dicalcium silicate (C_2S)	222	slow
Tricalcium aluminate (C_3A)	913	fast
Tetracalcium aluminoferrite (C_4AF)	306	moderate

Tricalcium silicate usually constitutes a large part of the Portland cement clinker. The exact proportion depends on the natural sources and the technology, approximately tricalcium silicate substitutes more than 60 % of the clinker [19]. As a result, the hydration of tricalcium silicate comprises a vast part of the heat developed during the hydration and hardening of cement paste. Thus, the graph for the generation of heat from tricalcium silicate is similar to the graph for the hydration of cement with a low content of aluminate minerals. Kalousek pinpointed this problem, which emerged to answer the reason for the dormant period after initial dissolution only by the silicate reaction. Kalousek proposed the formation of a protective calcium silicate hydrate layer around the clinker as an explanation for this period. Therefore, the description of the tricalcium silicate model became of special importance. Five stages are usually described during hydration of tricalcium silicate:

- Phase I: pre–induction
- Phase II: induction
- Phase III: hydration rate increase
- Phase IV: hydration rate decrease
- Phase V: low hydration rate

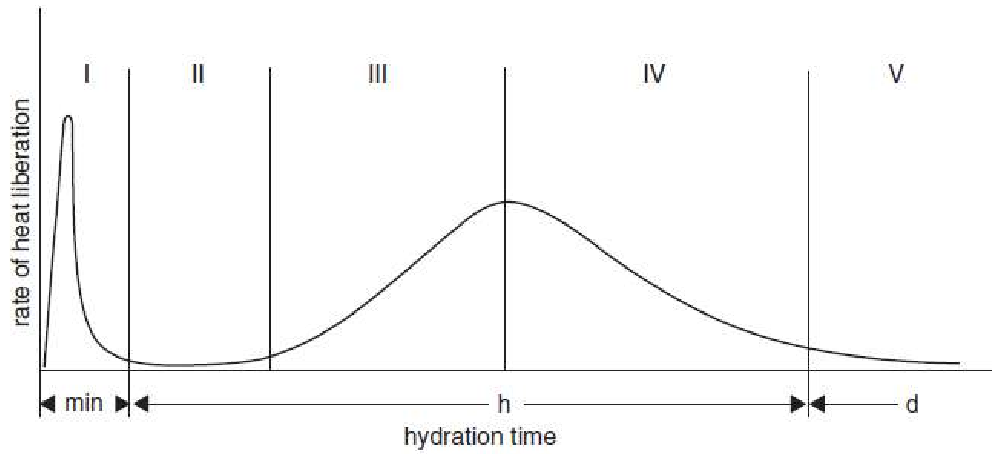

Figure 2.5: Description of tricalcium silicate hydration heat [19]

The first pre-induction period relates to the release of calcium cations and creation of a thin silicate layer resulting in the induction period. The mechanism of the induction period and its end is not unambiguously described. The possible explanation is the formation of nuclei on the surface for the growth of C-S-H. With increased hydration rate, the portlandite crystals and C-S-H significantly grow resulting in release of the heat. Later, the growth of the crystals and C-S-H slows down and the speed of released heat drops as well. The final stage corresponds to the low hydration rate.

Not only does the mineral composition influence the total amount and speed of heat liberation but also factors such as the fineness of the ground clinker particles or the water-cement ratio influence both, while the surrounding temperature or admixtures (retarders, accelerators) influence only the heat flux. Another option is to partly substitute the amount of the portland clinker with additives. To give an example, the hardening heat of the granulated blast furnace slag is low and reduces the total released heat. It also results in lower initial strengths.

To measure the released heat, isothermal calorimetry is a good option. The main principle is to capture the heat flow needed to keep the sample at the constant test temperature. This results in the plot of the heat released. The activation energy for the cement can be established by the set of measures within different temperatures. On the basis of the calculated hydration rate for the peaks of heat flow, the activation energy can be determined.

2.3 Techniques to reduce thermal cracks

All of the previous sections mainly concerned about the hydration heat of cement. The selection of the type and amount of cement is the most important parameter to decide on. In massive concrete structures, a good choice are type II cements where part of the portland cement is replaced by the admixtures. To decrease hydration heat, the use of fly ash or ground granulated blast furnace slag is very common. Unfortunately, this is often not enough and should be combined with other means of action described below. Very important is early preparation work of temperature control programme, which includes testing the concrete mixture recipes, choosing appropriate cooling technique, design and numerical testing of cooling plan and physical preparation of the technical parts of the system.

2.3.1 Pre-cooling of concrete

To reduce the maximum temperature of the concrete during hydration, the strongest influence is the initial placement temperature of the fresh concrete mixture. Reducing the placing temperature about 6 °C results in lowering of the maximum temperature about 3 °C. There are two main reasons for the maximum temperature reduction. Basically, lowering the initial temperature also lowers the final temperature. Furthermore, the hydration process rate decreases. To achieve a reasonable placement temperature, the most reasonable option is to reduce the temperature of key concrete substances. [1]

Table 2.2: Example of specific heat and total heat for mass concrete [1]

Ingredient	Batch weight kg	Specific heat $kJ \cdot kg^{-1} \cdot K^{-1}$	Batch heat content $kJ \cdot K^{-1}$
Coarse aggregate	1672	0.75	1254
Fine aggregate	528	0.75	396
Cement	117	0.88	103
Batch water	82	4.18	343

Quite often, an interest is put on the temperature of batch water. The main possibilities are to use cool water or to replace part of the water with ice. Of course, the specific heat of water is the highest of the substances; however, when considering the proportion, the initial temperature of the aggregate is also crucial. There are several options for aggregate from the easiest such as not using the aggregate from the top surface of the storage, shading of the storage, or conveyors to more developed such as spraying aggregate for evaporative cooling effect or immersion of the aggregate. [1]

The last key substance in concrete is cement. Normally, cooling of the cement is not applied in order to reduce the placement temperature due to the relatively low effect (relatively low proportion and specific heat). Furthermore, it could affect the properties of the cement if it is cooled below the dew point. Furthermore, it is necessary to consider the heat gains during the mixing and transportation of concrete. [1]

2.3.2 Formwork and concreting

The insulation of the formwork is essential in order to prevent surface cracks caused by the thermal gradient between the core part and the surface. Moreover, it reduces the negative effect of the ambient temperature, which is mostly significant during the downward-sloping part of the annual temperature cycle. The effect is intensified by short temperature drops during the nights. In a moderate climate, insulation with thermal resistance around 0.7 $m^2 \cdot K \cdot W^{-1}$ is efficient enough. This approximately corresponds to 30 mm of polystyrene or urethane with thermal conductivity around 0.03 - 0.04 $W{\cdot}m^{-1} \cdot K^{-1}$. For areas where short temperature drops are more probable, thicker insulation is recommended to reduce the risk of cracking. [1]

Horizontal surfaces are more difficult to effectively insulate due to the needs of construction workers. However, the importance is the same as that for the formed surfaces. The maximum efficiency of insulation provides pond water or a layer of sand in close contact with the surface. Another practical possibility is to apply roll-on mineral or glass wool blankets when the concrete is sufficiently hardened. Special attention should be paid to the edges and corners where heat can flow in more directions. Therefore, the vicinity of edges and corners is subjected to larger and earlier tensile strains. Increasing the thickness of the insulation at the edges and corners is reasonable for moderately large structures. When removing the formwork, attention should be paid to sudden drop in temperature. During cold weather, it can lead to initiation of the surface cracks. [1]

In addition to the formwork, interest could also be put to the casting time. The idea of night casting is to mainly decrease the placing temperature. On the other hand, the peak of hydration can meet higher afternoon temperatures. This should be carefully considered and planned.

2.3.3 Pipe cooling system

Another option to lower the peak temperature during hydration and deal with the hydration heat is to dissipate the heat away from the construction. An effective way is an embedded pipe cooling system with circulating medium. This system was adopted on a large scale first by the US Bureau of Reclamation during the construction of Hoover Dam in Colorado (1931-1936). Today, it is widely used and well adopted in Sweden. In recent years, this technique has been used in a few projects in Czechia. The pilot project employing this technique was the construction of the arch bridge over Oparno Valley [43] on the highway D8 (direction Prague-Dresden) during 2008 and 2011. In this case, pipe cooling system was used during arch ribs casting. It has been used in other projects, such as construction of Dvorecký Bridge (Prague), monolithic part of pedestrian bridge HolKa (Prague) [30] or for pylon of the bridge in Pardubice.

The most widely used medium is water because of its availability. Cool water from natural sources, e.g. wells or flowing streams, is possible to use when its supply is adequate and also meets other requirements. The temperature of this source should be reasonably constant and should not contain large amount of sediments. The water circulated through the cooling pipes is slightly warm, and depending on the local or national environmental codes, an allowance may be required to discharge water back to the source. The cooling system is divided to the loops with target length up to 250 m. For larger structures, placing the pipes in hexagonal pattern is optimal, see Figure 2.6. The horizontal spacing between pipes is usually within range of 1.5-3.0 m.[1; 10]

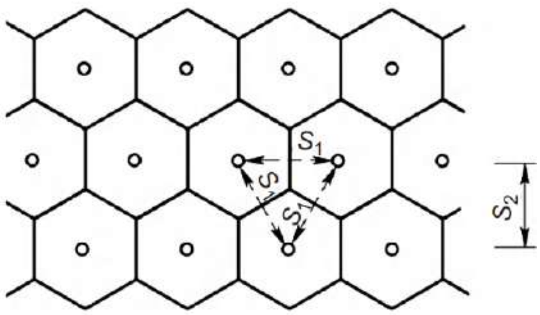

Figure 2.6: Hexagon arrangement of cooling pipes [10]

There are mainly two material possibilities, originally the steel thin walled pipes were used. High steel's conductivity ensures the fast controllability, but the installation is more laborious. Nowadays, the plastic materials such as HDPE (High density polyethylene) are frequently used. The temperature stability for pipe products from HDPE is up to 60 °C. Furthermore, it reduces material costs as well as the labour work. Disadvantage is low conductivity and slower controllability. It is also essential to minimise the number of splices within the pipe to ensure water tightness. In addition, its water tightness should be tested before casting. An important factor is also the water flow. When it is low, the water heats up faster, and for longer loops it can heat up to the concrete temperature and lose its functionality for a part. [1; 10]

In addition to the pipe system the parameters of the technical equipment are essential for operating the system. A pumping plant is essential to ensure the turbulent flow conditions which increase the rate of heat flow by convection within the medium. With a refrigeration plant, it is possible to cool down the water source. In addition, components such as filters, compressors, condensors, valves and others are usually used.

2.3.4 Pre-heating system

An alternative method to reduce thermal cracking is preheating the sublayer or previously cast sections by the embedded electrical wiring system. This approach allows the newly cast part to cool simultaneously with the heated adjoining section, ensuring similar deformation in both parts. As a result, stress development is significantly reduced. To ensure simultaneous deformation, the sublayer must be free to deform without any restraints. The pilot project in Sweden was the construction of the road tunnel under the main railway line at Ulriksdal, Stockholm, see Figure 2.7.

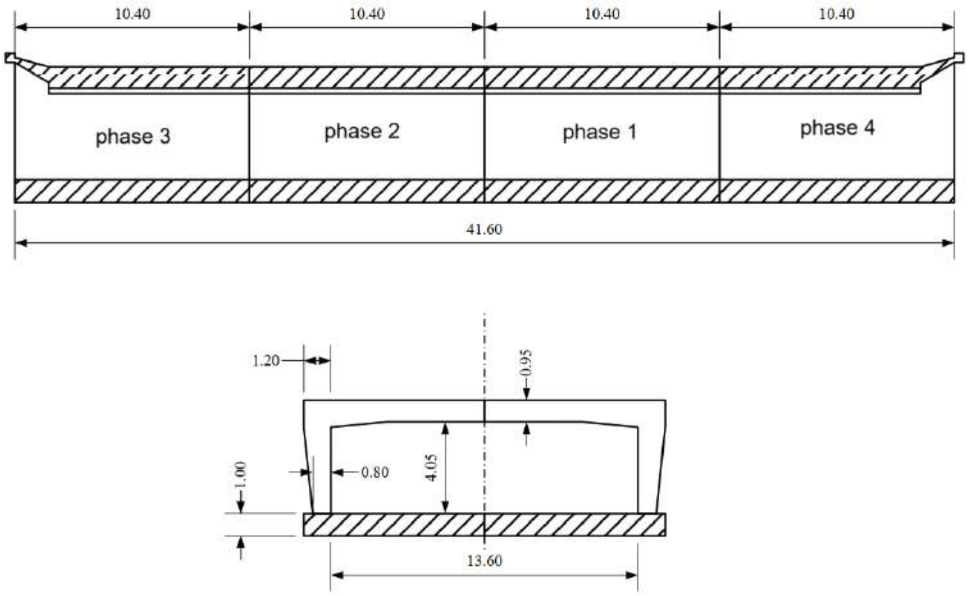

Figure 2.7: Geometry of the bridge near Ulriksdal [38]

The tunnel length is 41.6 m and its casting was divided into four monoliths. The maximum allowance for the crack width was 0.1 mm due to the fact that the groundwater level is 5.0 m above the foundation level. To reduce the risk of temperature cracks, heating the slab with embedded heating cables before and during the casting of walls and arch part was proposed and presented by the calculation performed in cooperation with Luleå University of Technology. This procedure was accepted by Banverket. The construction was cast during the winter of 1989-1990. The calculation performed after the casting emphasizes on comparison with pipe cooling for different season conditions. By numerical calculations, it has been proven that even during summer, a better choice is preheating compared to the pipe cooling. However, numerical analysis results indicate that pipe cooling is a viable option with higher risk of cracking. Other projects were realised with the use of the preheating technique after this pilot project. Specifically, the tunnel near Antuna, Upplands-Väsby or bridge over the railway in Älvsunda, Upplands-Väsby were built at the beginning of the 1990s.[38]

It should be noted that frame bridge structures, such as the bridge mentioned near Ulriksdal, are statically indeterminate structures. Therefore, these structures are more sensitive to temperature loading and especially to restraint conditions. This results in a higher stress level. In the case of preheating the sublayer, the restraint is significantly mitigated, whereas with the pipe cooling, it is not possible to mitigate restraint. Therefore, for indeterminate structures with complicated geometry and restraint conditions, preheating is more appropriate choice. The main reason is a better influence on the change of restraint conditions. The main drawback of this technique is the need to heat the entire previously cast section, which is highly impractical for large structures, such as massive blocks or foundations. In addition, factors such as local resource availability and overall cost must be considered. Given the current high electricity prices, pipe cooling becomes a more favourable alternative due to its practicality and efficiency.

2.4 Modelling approaches

The number of projects in the Czech Republic that use pipe cooling treatment can be counted on one's hands. The primary reason for this limited application is the number of large-scale projects, construction practice and also the lack of technology knowledge of companies. In contrast, the situation in Sweden is quite different. Pipe cooling has become a widely used and almost standard practice, reflecting a greater emphasis on temperature control in massive concrete structures due to factors such as colder climates, increased prevalence of large-scale projects requiring thermal crack mitigation, or better regulations. This led to the development of a methodology to mitigate the risk of cracking in early-aged concrete structures.

The requirements for civil engineering structures with respect to cracking are specified in *Bro 2004* issued by the Swedish Transport Administration (Trafikverket). In accordance with this regulation, three possible methods are:

- **Method 1:** Satisfying the predescribed requirements of Bro 2004.
- **Method 2:** Applying a predefined case-based solution according to Technical Report LTU 1997:02, "*Thermal Cracks in Concrete Structures Part A, B, and C*" (in Swedish: "*Temperatursprickor i betongkonstruktioner Del A, B och C*").

- **Method 3:** Performing numerical modelling and calculations.

The conditions described in *Bro 2004* consists of specification of temperature (air temperature and vapour) to eliminate the risk of surface cracks and through cracks. At the same time, requirements are set for the cement content, geometry, and interlocking. In addition, interactive Excel programme *CraX1* was created based on the first two methods. The results of the programme were calibrated against the numerical simulations.

The programme evaluates the risk of through cracks for a wall on a slab foundation. It is possible to change the geometry of the members. For this geometry wide range of problems can be simplified. Possible techniques implemented are the cooling of pipes or the preheating by electrical wiring. For the cooling pipes it is possible to choose between two different arrangements, two cooling powers and three different medium temperature. It is also able to align other parameters such as concrete class, cement amount, batch temperature, ambient temperature, restraint conditions or specify the thermal properties of formwork.

Chapter 3

Finite Element Analysis

According to the previously described methods, the most appropriate is numerical modelling and calculations. The most frequently used numerical method for structural applications is the finite element method (FEM). The origin of FEM dates back to 1943, when the main idea was formed by the mathematician R. Courant [13]. The first practical use of this method is related to aerospace engineering, when M.J. Turner emphasised its easier computer programmability compared to the contemporary force method [35]. With later broader availability of computer and increased computing power it has led to massive utility in a wide variety of engineering problems. Today, it allows us to calculate an approximate solution for complicated engineering problems described by partial differential equations. Its possibility to control the parameters of the model and also fast alignment of its parameters to ensure its similarity to reality is of key importance.

For more complicated and larger problems the use of object-orientated structure has the advantage of dividing the problem into the independent parts describing mesh, material, boundary conditions and solver preferences. It also allows the extension for the multi-physics problems. This theses uses the Object-Oriented Finite Element Method (OOFEM) software developed by the Department of Mechanics at CTU Faculty of Civil Engineering in Prague [24]. OOFEM is an open-source tool that supports coupled thermo-mechanical simulations, making it a suitable choice for this application.

Concrete is a complex composite material with properties and behaviour that vary significantly over time. In order to properly capture its behaviour, different mathematical models have been created. For this particular purpose of theses, a description of hydration, thermal properties, strength properties and cracking is essential. In addition, phenomena such as viscoelasticity, shrinkage, or creep greatly influence the results of the analysis. It is necessary to consider the above-mentioned phenomena in order to remain in close connection with the real behaviour of the structure. Therefore, the influence of these phenomena is accounted for in the analysis. In this part, the implemented material models and the principles of the FE procedure are presented.

3.1 Thermal analysis

The aim of thermal analysis is to determine the thermal field during the hydration and cooling process, which is a vital input for the following mechanical analysis. In this particular case, heat transfer is mainly driven by conduction within the particles of the concrete. The second law of thermodynamics says that energy (or heat) is transferred from particles with higher energy (warmer) to those with lower energy (colder) to reduce the energy difference. Feat flux $\mathbf{q}(\mathbf{x}, t)$, which describes the amount of heat transferred through the unit area, can be determined by Fourier's law:

$$\mathbf{q}(\mathbf{x}, t) = -\lambda \left\{ \begin{array}{c} \frac{\partial}{\partial x} \\ \frac{\partial}{\partial y} \\ \frac{\partial}{\partial z} \end{array} \right\} T(\mathbf{x}, t) = -\lambda \nabla T(\mathbf{x}, t) \tag{3.1}$$

where:

λ	is thermal conductivity parameter,
$\nabla T(\mathbf{x}, t)$	is vector of temperature gradients

According to Equation (3.1) the heat flux $\mathbf{q}(\mathbf{x}, t)$ has an opposite direction compared to the temperature gradient. An explanation comes from the fact that the direction of the temperature gradient is associated with increase in temperature, whereas the heat flux direction follows the flow of energy based on the second law of thermodynamics [5]. In terms of physics, the problem can be described as a transient heat transfer with an inner source of heat that corresponds to the hydration of cement. Based on the law of energy conservation and equilibrium of energy for infinitesimally small particle [5], it is possible to determine following parabolic partial differential equation:

$$\rho c \frac{\partial T(\mathbf{x}, t)}{\partial t} = \lambda \left(\frac{\partial^2 T(\mathbf{x}, t)}{\partial x^2} + \frac{\partial^2 T(\mathbf{x}, t)}{\partial y^2} + \frac{\partial^2 T(\mathbf{x}, t)}{\partial z^2} \right) + Q(\mathbf{x}, t) \tag{3.2}$$

where:

ρ	is density,
c	is thermal capacity,
$Q(\mathbf{x}, t)$	is function of heat source(due to hydration)

It is possible to solve this equation analytically for simple cases, but for more complicated cases, the solution becomes more difficult. An appropriate choice for solving this equation is the use of finite element software.

First, it is necessary to discretise geometry with a finite mesh. When reformulating the previously described differential equation to a weak form, applying boundary conditions and describing unknowns with its derivatives using the Galerkin approximation:

$$T(\mathbf{x},t) \approx \mathbf{N}(\mathbf{x})\mathbf{r}(t) \tag{3.3}$$

$$\frac{dT(\mathbf{x},t)}{d\mathbf{x}} \approx \frac{d\mathbf{N}(\mathbf{x})}{d\mathbf{x}}\mathbf{r}(t) = \mathbf{B}(\mathbf{x})\mathbf{r}(t) \tag{3.4}$$

where:

$\mathbf{N}(\mathbf{x})$	is matrix of shape functions,
$\mathbf{B}(\mathbf{x})$	are derivatives of shape function,
$\mathbf{r}(t)$	is vector of discrete temperature values

Then, it is possible to reach compound matrix formulation of the problem:

$$\mathbf{C}\dot{\mathbf{r}} + \mathbf{K}\mathbf{r} = \mathbf{f} \tag{3.5}$$

where:

$\mathbf{C}$	is global matrix of vsdensity->capacity,
$\mathbf{K}$	is global matrix of conductivity,
$\mathbf{f}$	is vector containing heat sources and boundary conditions

The above-mentioned matrices are described by shape functions $\mathbf{N}(\mathbf{x})$, first derivatives of shape functions $\mathbf{B}(\mathbf{x})$, and material parameters:

$$\mathbf{C} = \int_\Omega \rho c \mathbf{N}(\mathbf{x})^T \mathbf{N}(\mathbf{x}) d\Omega \tag{3.6}$$

$$\mathbf{K} = \int_\Omega \lambda \mathbf{B}(\mathbf{x})^T \mathbf{B}(\mathbf{x}) d\Omega \tag{3.7}$$

$$\mathbf{f} = \int_\Omega \mathbf{N}(\mathbf{x})^T Q(\mathbf{x},t) d\Omega \tag{3.8}$$

It yields to the system of linear differential equations of first order. The system of equations depends not only on geometry but also on time. Therefore, it is necessary to discretise the system to the final amount of time steps in which the equation is solved [9]. The temperature and its derivative are formulated according to:

$$\begin{aligned} T(\mathbf{x},t) &\approx \left(1 - \frac{t - t_{i-1}}{\Delta t}\right) T^i(\mathbf{x}) + \frac{t - t_{i-1}}{\Delta t} T^{i+1}(\mathbf{x}) = \\ &= (1-\alpha) T^i(\mathbf{x}) + \alpha T^{i+1}(\mathbf{x}) \end{aligned} \tag{3.9}$$

$$\frac{\partial T(\mathbf{x},t)}{\partial t} = \frac{1}{\Delta t}\left(T^{i+1}(\mathbf{x}) - T^i(\mathbf{x})\right) \tag{3.10}$$

When inset into the matrix formulation from Equation 3.5, it yields:

$$\left(\alpha\mathbf{K} + \frac{1}{\Delta t}\mathbf{C}\right)\mathbf{r}^{i+1} = (1-\alpha)\mathbf{f}^{i} + \alpha\mathbf{f}^{i+1} + \left(\frac{1}{\Delta t}\mathbf{C} - (1-\alpha)\mathbf{K}\right)\mathbf{r}^{i} \tag{3.11}$$

The parameter α influences the accuracy and stability of the solution [9]. Shorter time steps increase the accuracy of the solution; however, as the negative consequence, the computation time increases. Therefore, it is necessary to choose the time step carefully in accordance with the analysis. To ensure the stability of solution, the choice of parameter α should be within the interval $\alpha \in [0.5; 1]$ [9]. For parabolic PDE problems, the Crank-Nicholson method is often used, for which the value of parameter α is 0.5.

3.1.1 Thermal properties

It is very important to mention assumptions of the material model related to thermal analysis. Concrete is simplified to a homogenous and isotropic material with constant thermal properties over the time of analysis. This strong assumption is more or less correct. The **density** ρ and the **thermal capacity** c can be determined based on its mixture composition. Considering the properties of individual ingredients, the final properties of the mixture can be calculated as a weighted average according to the proportion of each component [10]. The thermal capacity for regular massive concrete is usually between 800 to 1170 $\mathrm{J \cdot kg^{-1} \cdot K^{-1}}$ [36].

Table 3.1: Thermal properties of mass concrete ingredients [10]

Material	**Density** ρ	**Conductivity** λ (W/(m·K))		**Specific Heat** c (kJ/(kg·K))	
	(kg/m^3)	21°C	54°C	21°C	54°C
Water	1000	0.600	0.600	4.187	4.187
Cement	3100	1.236	1.352	0.456	0.825
Quartz sand	2660	3.091	3.067	0.699	0.867
Granite gravel	2680	2.916	2.883	0.716	0.775
Lime gravel	2670	4.033	3.793	0.749	0.821
Quartz gravel	2660	4.700	4.580	0.691	0.791

The made assumption can be mainly discussed for the **thermal conductivity** λ, because significant variation during hydration was proven. It had been found out, thermal conductivity lowers from 20 up to 30 % compared with the initial value [31]. Usually, thermal conductivity for concrete is in range of 1.2 and 3.5 $\mathrm{Wm^{-1}K^{-1}}$ [37]. The range of thermal conductivity variation is also much higher compared to the thermal capacity range. This is mainly due to the large variation in conductivity for the aggregate. The described variation range for specific heat and conductivity is in accordance with the thermal parameters determined for large conventional dams according to Bofang [10].

3.1.2 Approximation of hydration

A key aspect of the material model is the description of the amount of heat released, which is closely related to the hydration process. For this analysis, the implemented *HydratingConcreteMat* model is used. This model allows for either an exponential or an affinity approximation of hydration [26]. The exponential approximation is easier to calibrate against experimental data and suitable for simpler models. In contrast, the affinity model, while more complex due to additional parameters, is based on a more precise chemical description of hydration, providing a more accurate representation of hydration kinetics. Thus, the affinity approximation is preferred for this analysis.

The affinity model is inspired by the analytical form of the normalised affinity model proposed by Cervera [12]. The reference temperature for the modified model is set to 25 °C [26]. A slightly modified formulation of isothermal hydration is as follows:

$$\tilde{A}_{25}(DoH) = B_1\left(\frac{B_2}{DoH_\infty} + DoH\right)(DoH_\infty - DoH)\exp\left(-\bar{\eta}\frac{DoH}{DoH_\infty}\right) \tag{3.12}$$

where:

B_1, B_2	are coefficients to be calibrated,
DoH_∞	is the ultimate hydration degree,
$\bar{\eta}$	represents microdiffusion of free water through formed hydrates

To account for the effect of arbitrary temperature T, Arrhenius equation scales the affinity function [26]. The degree of hydration is then the derivatives according to time:

$$\frac{\mathrm{d}DoH}{\mathrm{d}t} = \tilde{A}_{25}(DoH)\exp\left[\frac{E_a}{R}\left(\frac{1}{273.15+25} - \frac{1}{T}\right)\right] \tag{3.13}$$

where:

E_a	is activation energy,
R	is universal gas constant (8.314 $\mathrm{Jmol^{-1}K^{-1}}$)

Then, the total amount of released hydration heat is expressed according to:

$$Q(t) = m_{cem} DoH Q_{pot} \tag{3.14}$$

where:

m_{cem}	is cement mass per cubic metre,
Q_{pot}	is potential heat of hydration

The cement mass represents the active part of the material, acting as the heat source. Based on the element's volume and cement content, the released heat can be calculated. The asymptotic degree of hydration, DoH_∞, is set to 0.85, meaning that 85 % of the potential heat of hydration, Q_{pot}, is released over an infinite time. Consequently, these two parameters are interdependent. The potential heat of hydration is strongly influenced by the cement type. In this case, blended cement CEM II B-S was used. Approximate values for the potential heat of hydration and activation energy can be found in the literature [34].

Table 3.2: Affinity model parameters

Cement Type	**Affinity Model Parameters**					
	DoH_∞ -	Q_{pot} kJ/kg	E_a kJ/mol	B_1 h^{-1}	B_2 -	$\bar{\eta}$ -
CEM II B-S 32.5R	0.85	420	45.0	7.379 e-1	1.488 e-3	7.422

The remaining three parameters that describe the affinity model are calibrated against the previously measured isothermal calorimetry results data. The parameters are found with the provided script using the SciPy's optimise module in Python. The assumed values of the parameters are presented in Table 3.2, and the approximation of the heat released to the isothermal calorimetry results in Figure 3.1.

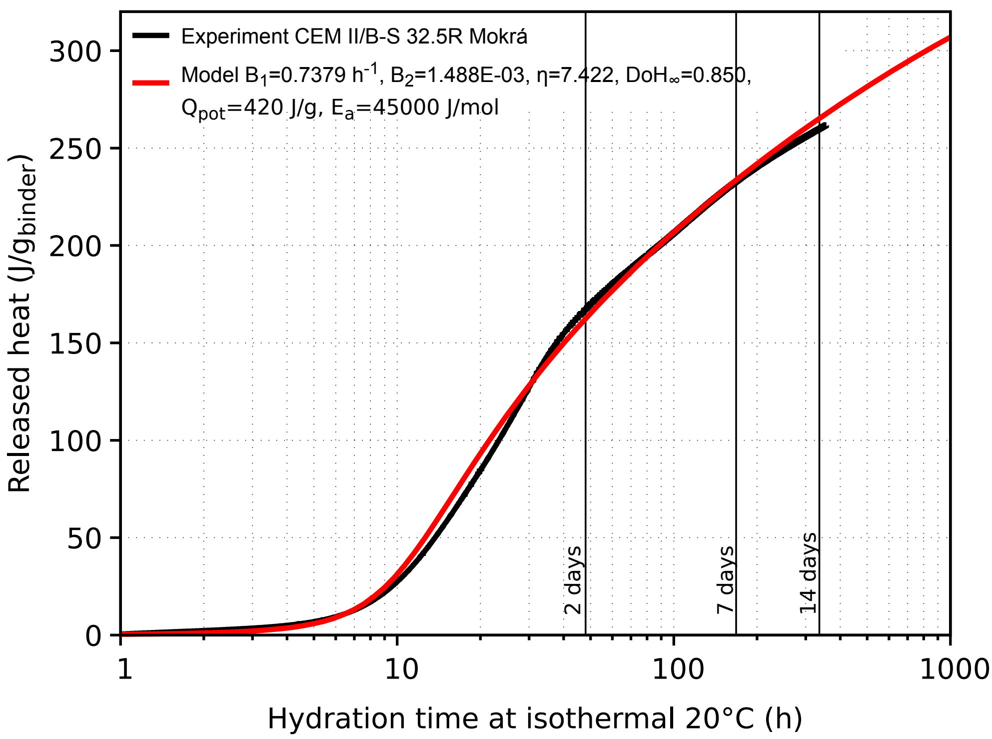

Figure 3.1: Affinity approximation of isothermal hydration

3.1.3 Initial and boundary conditions

To ensure the accuracy and reliability of the analysis, it is essential to define initial and boundary conditions that closely represent real conditions. These conditions serve as fundamental constraints that influence the solution of the problem, describing how the system behaves over time. In the context of finite element analysis, properly defined boundary and initial conditions are crucial for obtaining physically meaningful and numerically stable results. Thus, correctly chosen initial and boundary conditions ensure the fidelity of the model.

The initial conditions define the default state of the thermal field, describing the starting point of the analysis. The temperature distribution at the beginning of the simulation can vary due to the concreting process. In reality, large structural elements are never cast all at once. Instead, the casting process takes place over several hours. Consequently, the temperature naturally varies within the cast part, and the initial temperature distribution should ideally account for this variation. However, if the initial uniform temperature T_0 is set precisely, a reasonable level of accuracy can still be achieved. The format of the initial conditions follows:

$$T(\mathbf{x}, 0) = T_0 \tag{3.15}$$

If the boundary condition is not defined, heat exchange is not accounted for, resulting in a heat flux of zero [10]. Consequently, the model would be entirely insulated and behave as an adiabatic system. However, in the case of an axis of symmetry, the heat flux is naturally zero due to the geometric and thermal symmetry of the problem. The simplest boundary condition is the Dirichlet type, which is used to describe the temperature of the cooling pipe's water. Therefore, Dirichlet (first) type of boundary condition [10] describes the temperature at the bound Γ:

$$T(\mathbf{x}, t) = T_\Gamma(t) \tag{3.16}$$

Neumann (second) type of boundary condition [10] describes the rate of heat flux in direction of normal n on the boundary Γ:

$$-\lambda \frac{\partial T(\mathbf{x}, t)}{\partial n} = q_\Gamma(\mathbf{x}, t) \tag{3.17}$$

To describe the heat exchange between the surface of the cast construction and the environment, the suitable solution is the Newton (third) type of boundary condition [10]. For this condition, it is also necessary to specify the coefficient of heat transfer between the surface and the environment a. When modelling only the concrete part without additional insulation, it is necessary to take into account the effect of insulation on this coefficient. Newton boundary condition follows:

$$-\lambda \frac{\partial T(\mathbf{x}, t)}{\partial n} = a(T_s - T_a) \tag{3.18}$$

where:

a	is the coefficient of heat transfer between surface and environment,
T_s	is surface temperature,
T_a	is ambient temperature

In OOFEM it is possible to define Neumann and Newton boundary conditions with using *ConstantSurfaceLoad* and specifying the value of *loadType*. Neumann boundary condition is described by *loadType 2*, respectively Newton boundary condition by *loadType 3* [27]. Moreover, it is possible to adjust boundary conditions according to time by describing *loadTimeFunction* as well as the time-dependent behaviour of properties with *propertytf*. It is possible to describe time functions by user using *UsrDefLTF*, which supports regular mathematical functions.

3.2 Mechanical analysis

With a similar approach as in thermal analysis, it is possible to derive the finite element formulation for structural analysis by minimising the total potential energy of the system, which is governed by the relationship between displacement, strain, stress and external forces. The relationship between the displacements $\mathbf{u}(x, y, z)$ and strains $\boldsymbol{\varepsilon}$ can be described by kinematic equations, which in engineering practise can be written in vector form:

$$\boldsymbol{\varepsilon} = \begin{Bmatrix} \varepsilon_x \\ \varepsilon_y \\ \varepsilon_z \\ \gamma_{xy} \\ \gamma_{xz} \\ \gamma_{yz} \end{Bmatrix} = \begin{Bmatrix} \frac{\partial u}{\partial x} \\ \frac{\partial v}{\partial y} \\ \frac{\partial w}{\partial z} \\ \frac{\partial u}{\partial y} + \frac{\partial v}{\partial x} \\ \frac{\partial u}{\partial z} + \frac{\partial w}{\partial x} \\ \frac{\partial v}{\partial z} + \frac{\partial w}{\partial y} \end{Bmatrix} \tag{3.19}$$

In the previous equation the Voigt notation is used, because it is a convenient way to represent symmetric second-order tensors as vectors. It reduces complexity while maintaining accuracy. It should be noted that the strain components are determined from the displacement gradient $\nabla\mathbf{u}(x, y, z)$ which corresponds to the strain and rotation components. Because rigid body rotations do not contribute to strain, the strain tensor is obtained by symmetrising the displacement gradient:

$$\boldsymbol{\varepsilon} = \nabla^s\mathbf{u}(x) = \boldsymbol{\varepsilon} = \frac{1}{2}\left(\nabla\mathbf{u} + (\nabla\mathbf{u})^T\right) \tag{3.20}$$

$$\boldsymbol{\varepsilon} = \begin{bmatrix} \varepsilon_{xx} & \varepsilon_{xy} & \varepsilon_{xz} \\ \varepsilon_{yx} & \varepsilon_{yy} & \varepsilon_{yz} \\ \varepsilon_{zx} & \varepsilon_{zy} & \varepsilon_{zz} \end{bmatrix} = \begin{bmatrix} \frac{\partial u}{\partial x} & \frac{1}{2}\left(\frac{\partial u}{\partial y} + \frac{\partial v}{\partial x}\right) & \frac{1}{2}\left(\frac{\partial u}{\partial z} + \frac{\partial w}{\partial x}\right) \\ \frac{1}{2}\left(\frac{\partial u}{\partial y} + \frac{\partial v}{\partial x}\right) & \frac{\partial v}{\partial y} & \frac{1}{2}\left(\frac{\partial v}{\partial z} + \frac{\partial w}{\partial y}\right) \\ \frac{1}{2}\left(\frac{\partial u}{\partial z} + \frac{\partial w}{\partial x}\right) & \frac{1}{2}\left(\frac{\partial v}{\partial z} + \frac{\partial w}{\partial y}\right) & \frac{\partial w}{\partial z} \end{bmatrix} \tag{3.21}$$

Therefore, the shear strains in Voigt notation, which correspond to the angular deformations of planes, are derived from the symmetric strain tensor components. Thus, for the xy-plane, the engineering shear strain is given by:

$$\gamma_{xy} = \varepsilon_{xy} + \varepsilon_{yx} \tag{3.22}$$

The relation between the strain components and stresses is governed by the constitutive equations:

$$\boldsymbol{\sigma} = \mathbf{D}\boldsymbol{\varepsilon} \tag{3.23}$$

where:

$\boldsymbol{\sigma}$	is vector of stress components,
$\mathbf{D}$	is material stiffness matrix
$\boldsymbol{\varepsilon}$	is vector of strain components

The material stiffness matrix can be determined on the generised Hooke's law for 3D continuum, which in Voigt notation is simplified to 6×6 matrix:

$$\mathbf{D} = \frac{E}{(1+\nu)(1-2\nu)} \begin{bmatrix} 1-\nu & \nu & \nu & 0 & 0 & 0 \\ \nu & 1-\nu & \nu & 0 & 0 & 0 \\ \nu & \nu & 1-\nu & 0 & 0 & 0 \\ 0 & 0 & 0 & \frac{1}{2(1-2\nu)} & 0 & 0 \\ 0 & 0 & 0 & 0 & \frac{1}{2(1-2\nu)} & 0 \\ 0 & 0 & 0 & 0 & 0 & \frac{1}{2(1-2\nu)} \end{bmatrix} \tag{3.24}$$

and the stress vector components consist of:

$$\boldsymbol{\sigma} = \begin{Bmatrix} \sigma_x \\ \sigma_y \\ \sigma_z \\ \tau_{xy} = \tau_{yx} \\ \tau_{xz} = \tau_{zx} \\ \tau_{yz} = \tau_{zy} \end{Bmatrix} \tag{3.25}$$

Then, the balance of the external forces and internal stresses within the continuum is governed by the static equilibrium equations:

$$\begin{cases} \frac{\partial \sigma_{xx}}{\partial x} + \frac{\partial \sigma_{xy}}{\partial y} + \frac{\partial \sigma_{xz}}{\partial z} + f_x = 0 \\ \frac{\partial \sigma_{yx}}{\partial x} + \frac{\partial \sigma_{yy}}{\partial y} + \frac{\partial \sigma_{yz}}{\partial z} + f_y = 0 \\ \frac{\partial \sigma_{zx}}{\partial x} + \frac{\partial \sigma_{zy}}{\partial y} + \frac{\partial \sigma_{zz}}{\partial z} + f_z = 0 \end{cases} \tag{3.26}$$

As a consequence of the above relationships, the strong formulation of the problem describing the displacement vector $\mathbf{u}(x, y, z)$ and external forces in compact form follows:

$$\nabla \cdot \left(\mathbf{D}\left(\nabla^s \mathbf{u}(x, y, z) - \boldsymbol{\varepsilon}^0(x, y, z)\right)\right) + \bar{\mathbf{f}}(x, y, z) = 0 \tag{3.27}$$

where:

$\boldsymbol{\varepsilon}^0(x, y, z)$	is the initial strain vector,
$\bar{\mathbf{f}}(x, y, z)$	is the external force (body force) vector

Furthermore, the essential boundary conditions on Γ_u describe prescribed displacements or natural boundary conditions represent prescribed surface tractions $\bar{\mathbf{p}}(x, y, z)$ on the boundary Γ_p follows:

$$\Gamma_u \quad \Rightarrow \quad \mathbf{u}(x, y, z) - \bar{\mathbf{u}}_0(x, y, z) = 0 \tag{3.28}$$

$$\Gamma_p \quad \Rightarrow \quad \mathbf{n}(x, y, z) \cdot \left(\mathbf{D}\left(\nabla^s \mathbf{u}(x, y, z) - \boldsymbol{\varepsilon}^0(x, y, z)\right)\right) - \bar{\mathbf{p}}(x, y, z) = 0 \tag{3.29}$$

The weak form of the problem can be obtained by applying the principle of virtual work to the strong formulation (3.27). This requires multiplying the equilibrium equation by the virtual displacement $\delta \mathbf{u}$ and integrating over the domain Ω. When applying the integration by parts, the corresponding form is reached:

$$\int_\Omega \delta \boldsymbol{\varepsilon} : \mathbf{D}(\boldsymbol{\varepsilon} - \boldsymbol{\varepsilon}^0)\, d\Omega = \int_\Omega \delta \mathbf{u} \cdot \bar{\mathbf{f}}\, d\Omega + \int_{\Gamma_p} \delta \mathbf{u} \cdot \bar{\mathbf{p}}\, d\Gamma \tag{3.30}$$

where:

$\delta \boldsymbol{\varepsilon} = \nabla^s \delta \mathbf{u}$	is the virtual strain vector,
$\boldsymbol{\varepsilon} = \nabla^s \mathbf{u}$	is the actual strain vector

In the finite element method, the displacement $\mathbf{u}$ and also virtual displacement $\delta \mathbf{u}$ are approximated with the shape functions and vector of nodal displacements $\mathbf{d}$:

$$\mathbf{u} \approx \sum_{i=1}^{n} N_i \mathbf{d}_i = \mathbf{N}\mathbf{d} \tag{3.31}$$

$$\delta\mathbf{u} \approx \sum_{i=1}^{n} N_i \delta\mathbf{d}_i = \mathbf{N}\delta\mathbf{d} \tag{3.32}$$

where:

$\mathbf{N}$	is the matrix of shape functionsN_i,
$\mathbf{d}$	is the vector of nodal displacements,
n	is the number of nodes for the element

Similarly, the strain vector and virtual strain is related to the displacement by:

$$\boldsymbol{\varepsilon} = \nabla^s \mathbf{u} = \nabla^s \mathbf{N}\mathbf{d} = \mathbf{B}\mathbf{d} \tag{3.33}$$

$$\delta\boldsymbol{\varepsilon} = \mathbf{B}\delta\mathbf{d}. \tag{3.34}$$

where:

$\mathbf{B}$ is the matrix of shape functions derivatives

When inserting the determined relations to the original weak form of the problem 3.30, the following formulation is reached:

$$\int_{\Omega} (\mathbf{B}\delta\mathbf{d})^T \mathbf{D}(\mathbf{B}\mathbf{d} - \boldsymbol{\varepsilon}^0)\, d\Omega = \int_{\Omega} (\mathbf{N}\delta\mathbf{d})^T \bar{\mathbf{f}}\, d\Omega + \int_{\Gamma_p} (\mathbf{N}\delta\mathbf{d})^T \bar{\mathbf{p}}\, d\Gamma \tag{3.35}$$

Since $\delta\mathbf{d}$ is arbitrary, the finite element formulation of the system follows:

$$\int_{\Omega} \mathbf{B}^T\mathbf{D}\mathbf{B}\mathbf{d}\, d\Omega - \int_{\Omega} \mathbf{B}^T\mathbf{D}\boldsymbol{\varepsilon}^0\, d\Omega = \int_{\Omega} \mathbf{N}^T\bar{\mathbf{f}}\, d\Omega + \int_{\Gamma_p} \mathbf{N}^T\bar{\mathbf{p}}\, d\Gamma \tag{3.36}$$

where:

$$\mathbf{K} = \int_{\Omega} \mathbf{B}^T\mathbf{D}\mathbf{B}\, d\Omega \qquad \text{global stiffness matrix,} \tag{3.37}$$

$$\mathbf{F} = \int_{\Omega} \mathbf{N}^T\bar{\mathbf{f}}\, d\Omega \qquad \text{global body force vector,} \tag{3.38}$$

$$\mathbf{F}_p = \int_{\Gamma_p} \mathbf{N}^T\bar{\mathbf{p}}\, d\Gamma \qquad \text{global traction force vector,} \tag{3.39}$$

$$\mathbf{F}_0 = \int_{\Omega} \mathbf{B}^T\mathbf{D}\boldsymbol{\varepsilon}^0\, d\Omega \qquad \text{global force contribution of initial strains} \tag{3.40}$$

In engineering practice, the global matrices described above are typically computed using numerical integration over all elements in the system. This leads to the standard matrix formulation of the finite element method:

$$\mathbf{K}\mathbf{d} = \mathbf{F} + \mathbf{F}_p + \mathbf{F}_0 \tag{3.41}$$

The system of equations can be solved using standard matrix solution techniques. The finite element formulation provided above is valid only for linear analysis, where the geometry, material behaviour and boundary conditions of the structure are assumed to remain constant over time. However, when nonlinearity is introduced, such as in this case non-linear material models, to be more specific visco-elasticity and fracture behaviour. Consequently, the material stiffness matrix $\mathbf{D}$ described by constitutive equations and global stiffness matrix $\mathbf{K}$ are not constant over the analysis. As a result, it is not possible to solve the system of equations with direct methods. Instead, an appropriate iterative method needs to be employed to achieve convergence and accuracy in the solution. In this case, the Newton-Raphson method is accommodated. The FE formulation for the linear problem (3.41) can be rewritten to the form, where left side corresponds to the internal force and right side to the external force:

$$\mathbf{f}_{\text{int}}(\mathbf{d}^{(i)}) = \mathbf{f}_{\text{ext}} \tag{3.42}$$

The principal of the Newton-Raphson method is the iterative procedure:

$$\mathbf{K}^{(i-1)}\delta\mathbf{d}^{(i)} = \mathbf{f}_{\text{ext}}^{(i)} - \mathbf{f}_{\text{int}}^{(i-1)} \tag{3.43}$$

$$\mathbf{d}^{(i)} = \mathbf{d}^{(i-1)} + \delta\mathbf{d}^{(i)} \tag{3.44}$$

Here, $\mathbf{K}$ is the tangent stiffness matrix, which accounts for the non-linear behaviour. The tangent stiffness matrix is recalculated in each iteration step, see different slopes of $\mathbf{K}_0$ and $\mathbf{K}_1$ in Figure 3.2. The residual force vector $\mathbf{R}$, defined as the difference between the internal and external force vectors, is monitored during the iterative process. Once residual falls within the specified tolerance, the solution is considered converged and the iterative procedure is terminated. This convergence criterion follows:

$$\frac{||\mathbf{f}_{\text{ext}} - \mathbf{f}_{\text{int}}^{(i)}||}{||\mathbf{f}_{\text{ext}} - \mathbf{f}_{\text{int}}^{(i-1)}||} < \epsilon_R \tag{3.45}$$

Usually, convergence should also satisfy the criterion that the norm of the displacement increment vector is sufficiently small compared to the norm of the total displacement vector:

$$\frac{\|\Delta \mathbf{d}^{(i)}\|}{\|\mathbf{d}^{(i)}\|} < \epsilon_d \tag{3.46}$$

where:

ϵ is the convergence tolerance limit

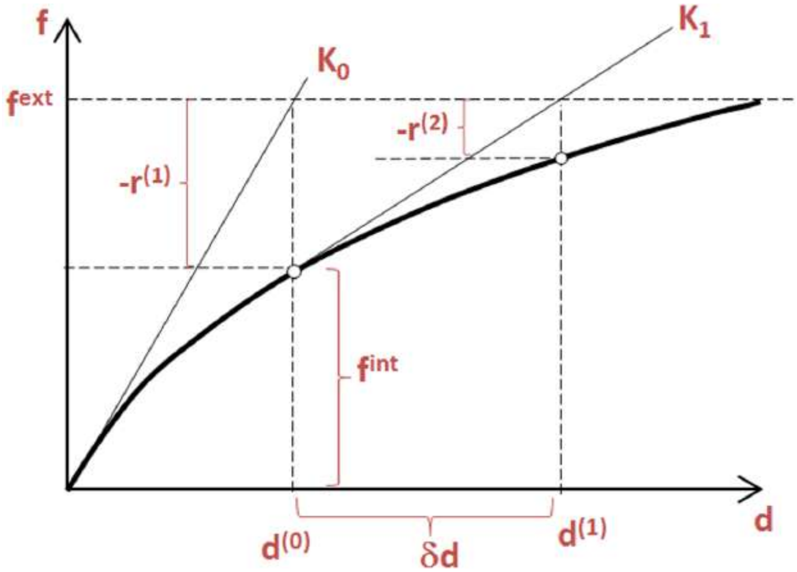

Figure 3.2: Newton-Raphson method, source Scia Engineer 19 Manual [32]

3.3 Material models

Since the material model used for the thermal analysis has already been described in Section **Thermal analysis**, this section focuses exclusively on the material models assumed for the description of mechanical behaviour.

3.3.1 Concrete strength

Since the analysis is performed from the initial stages of casting, it is essential to account for the time-dependent development of material properties, particularly tensile strength. The evolution of tensile strength is of primary importance, as massive concrete structures are generally more susceptible to tensile cracking than to compressive failure. This is due to the low tensile capacity of concrete relative to its compressive strength, combined with internal stresses induced mainly by hydration heat and shrinkage. Accurately modelling the gradual increase in tensile strength over time is therefore crucial for predicting crack initiation and propagation.

In OOFEM it is possible to assume the time-development of the tensile strength by modification of the *fib* MC2010[15] with *timeDepFracturing* [26]. It requires to specify the value of *fib_s* which is determined based on the strength class and hardening characteristic of used cement. According to the Table 3.3 for the used cement class 32.5 R, s = 0.25.

Table 3.3: Coefficient s for different cement types, Table 5.1-9 *fib* MC2010[15]

Strength class of cement	32.5 N	32.5 R 42.5 N	42.5 R 52.5 N 52.5 R
s	0.38	0.25	0.20

Moreover, the tensile strength at 28 days should be specified, this corresponds to parameter *ft28*. Based on this tension strength, it is possible to determine characteristic compressive strength, respectively mean compressive strength:

$$f_{\text{ctm}} = 0.3(f_{\text{ck}})^{2/3} \tag{3.47}$$

$$f_{\text{cm}} = f_{\text{ck}} + 8 \tag{3.48}$$

Then, the current mean compressive strength at time t for reference temperature of 20 °C is possible to calculate based on the[15]:

$$f_{\text{cm}}(t) = \beta_{\text{cc}}(t) \cdot f_{\text{cm}} \tag{3.49}$$

$$\beta_{\text{cc}}(t) = \exp\left\{ s \cdot \left[1 - \left(\frac{28}{t} \right)^{0.5} \right] \right\} \tag{3.50}$$

where:

$\beta_{\text{cc}}(t)$	is a function to describe the development with time
t	is the concrete age at days with the temperature influence

It is essential to determine the mean value of compressive strength, because the tensile strength is assumed in accordance with it corresponding to [26]:

for 0 MPa $\leq f_{\text{cm}}(t) \leq$ 20 MPa $\quad f_{\text{tm}}(t) = 0.015 \cdot 12^{\frac{2}{3}} f_{\text{cm}}(t)$ (3.51)

for 20 MPa $\leq f_{\text{cm}}(t) \leq$ 58 MPa $\quad f_{\text{tm}}(t) = 0.3\,(f_{\text{cm}}(t) - 8)^{\frac{2}{3}}$ (3.52)

and finally for $f_{\text{cm}}(t) > 58$ MPa $\quad f_{\text{tm}}(t) = 2.12 \ln (1 + 0.1 f_{\text{cm}}(t))$ (3.53)

3.3.2 Concrete creep and shrinkage

As previously discussed, cracking in concrete is not solely caused by overloading. Due to the inherent complexity of the material, its behaviour is significantly time-dependent. Although an earlier section has examined the time-dependent development of tensile strength, it is also important to recognise that Young's modulus also evolves over time. Furthermore, phenomena such as shrinkage and creep can contribute to undesired cracking, particularly in restrained or massive structures.

To account for these effects, concrete is commonly modelled as an ageing viscoelastic material. Rheology provides the theoretical framework for describing such time-dependent behaviour. In particular, basic creep refers to the strain that develops under a sustained stress state, assuming constant humidity and temperature. The second part of the total creep is drying creep caused by the transfer of the moisture from the structure element to the environment. Although the rate of creep decreases as the material ages, there is no defined upper limit to the total strain that may develop over time in practical applications.

To deal with the description of creep two different approaches exist. The first and simpler is the description provided by the design standards such as Eurocode 2: Design of concrete structures [14] or *fib* MC 2010 [15]. These codes work with the creep coefficient, denoted as $\varphi(t, t_0)$, which is a dimensionless parameter that characterises the time-dependent increase in strain under a sustained constant stress σ applied at time t_0. It is defined as the ratio between the creep strain $\varepsilon_{\mathrm{cc}}(t, t_0)$ and the instantaneous elastic strain $\varepsilon_{\mathrm{e}}(t_0)$ at the time of loading:

$$\varphi(t, t_0) = \frac{\varepsilon_{\mathrm{cc}}(t, t_0)}{\varepsilon_{\mathrm{e}}(t_0)} = \frac{\varepsilon_{\mathrm{c}\sigma}(t) - \varepsilon_{\mathrm{e}}(t_0)}{\varepsilon_{\mathrm{e}}(t_0)} \tag{3.54}$$

Consequently, the stress-dependent strain (instantaneous and creep) at time t is expressed as:

$$\varepsilon_{\mathrm{c}\sigma}(t) = \sigma(t_0)\left(\frac{1}{E_{\mathrm{c}}(t_0)} + \frac{\varphi(t, t_0)}{E_{\mathrm{c}}}\right) \tag{3.55}$$

The creep coefficient is influenced by a range of parameters, including the age at loading t_0 concrete strength class, cement type, cross-sectional geometry and relative humidity. When using the extended formulations provided in Annex B of Eurocode 2 [14], it is also possible to account for the effects of ambient temperature, time-variable loading history and ageing. These extensions improve the applicability of the creep coefficient method for more realistic structural behaviour.

It is important to note that design standards typically consider only linear creep behaviour. According to Eurocode2[14], the compressive stress should not exceed 0.45 $f_{\mathrm{ck}}(t_0)$, while the fib Model Code 2010 [15] recommends a slightly more conservative limit of 0.40 $f_{\mathrm{ck}}(t_0)$. Both standards also provide empirical formulations for estimating autogenous and drying shrinkage.

While these design code approaches are well-suited for typical engineering applications, they may lack the accuracy required for civil engineering structures of special importance or those subjected to complex environmental and loading conditions. In such cases, more advanced and physically-based models, such as Bažant's B3 model [6], offer improved fidelity. Advanced models operate with more general creep compliance function $J(t, t_0)$ to capture the time-dependent viscoelastic response. The total strain then corresponds to:

$$\varepsilon_{c\sigma}(t) = \sigma(t_0) \cdot J(t, t_0) \tag{3.56}$$

In practical engineering applications, concrete is frequently idealised as an ageing linear viscoelastic material. Within this framework, the principle of superposition proves particularly useful when addressing variable stress and strain histories. Based on these assumptions, and the definitions introduced above, the constitutive relationship for concrete can be formulated as [15]:

$$\varepsilon_{c\sigma}(t) = \sigma(t_0) J(t, t_0) + \int_{t_0}^{t} J(t, \tau) \frac{\partial \sigma(\tau)}{\partial \tau} \, d\tau \tag{3.57}$$

Advanced models require a more extensive set of input parameters, including details of the concrete mixture composition, curing conditions and environmental exposure, in order to achieve proper calibration. Model B3 is based on the more physically meaningful origin. The principle of this model lies on a solidification theory proposed by Bažant earlier. A limitation of the model B3 lies in its simplified treatment of temperature effects. This reduces its applicability in thermally complex scenarios, such as massive concrete structures, where non-uniform temperature fields and the progression of hydration significantly influence mechanical behaviour.

The B3 model, originally introduced by Bažant and Baweja in 1995 [6], represented a significant advancement in the modelling of concrete creep and shrinkage by incorporating the effects of ageing, humidity and cement composition. Since its initial formulation, several enhancements have been made, driven in part by increased computational capabilities that allow the implementation of more complex constitutive laws. This ongoing development led to the creation of the Microprestress-Solidification (MPS) theory [7], also initiated by Bažant, which extends the B3 model by capturing micro-level prestress effects resulting from moisture and temperature changes. The most recent formulation [18], updated by Jirásek and Havlásek, introduces improved modelling of temperature and humidity interactions and enables integration into the OOFEM simulation environment. Owing to these advancements and the model's capacity to simulate long-term time-dependent behaviour under varying environmental conditions, the MPS theory is employed in this analysis as a robust framework for representing the mechanical response of concrete.

3.3.3 Microprestress-Solidification theory

As a simplification, the assumed rheological model incorporating the Microprestress Solidification (MPS) theory can be represented through several components arranged in series, see Figure 3.3. This includes a non-ageing elastic spring accounting for the instantaneous elastic deformation ε_a, a solidifying Kelvin chain that captures the short-term creep ε_v and an ageing dashpot with viscosity influenced by microprestress S to describe deformation of long-term creep ε_f. In addition, units simulating deformation caused by shrinkage ε_sh and thermal expansion ε_T are attached. Thus, the total strain is obtained as the sum of the individual strain contributions from each element, while the stress is equal across all components due to serial configuration. However, this decomposition is a modelling simplification, it enables a computationally feasible approximation of the complex viscoelastic behaviour of concrete. [18]

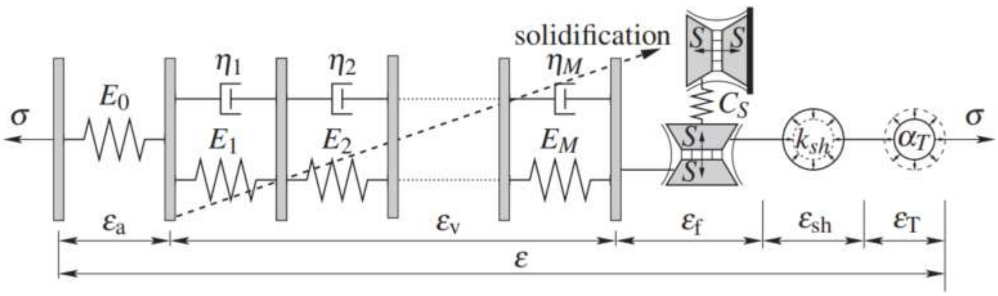

Figure 3.3: Rheological scheme of the MPS model [18]

It is important to note that the elements of this rheological chain should not be interpreted as actual physical constituents. Notably, the so-called asymptotic modulus used for the instantaneous elastic spring is not equivalent to the standard static modulus. Instead, it reflects to the response at very short time interval and its value is derived through extrapolation of experimental data. The Kelvin chain used for short-term creep modelling is selected because of its mathematical suitability to represent the compliance function using a Dirichlet series. This approach allows different terms in the series to effectively approximate various parts of the retardation spectrum. [18]

Furthermore, concrete is a heterogeneous material in which creep occurs almost exclusively within the cement paste, while the aggregates retain the elastic behaviour [18]. This heterogeneity can be better captured through multiscale or micromechanical approaches, however such models require more input data related to the microstructure of the material and are not always practical for engineering applications. The model used in the MPS theory offers a great ratio between accuracy and usability, particularly for large-scale structural analyses.

In practice, experimental data often distinguish mechanical strain from shrinkage and thermal strains. Therefore, it is usually measured separately on load-free laboratory specimens. However, the evolution of strain remains affected by environmental conditions, particularly humidity and temperature. Although drying reduces the overall magnitude of creep, it accelerates transitional creep [18]. Similarly, elevated temperatures speed up cement hydration and reduce compliance due to faster ageing, but also enhance viscous flow mechanisms and accelerate microprestress relaxation [18]. These influences highlight the necessity of including environmental coupling within MPS model. In the case of OOFEM it is controled with specification of *CoupledAnalysisType* [26]. In this case, the model is coupled only with the thermal analysis, thus the *CoupledAnalysisType* 3 is set.

The basic creep compliance function of the MPS model corresponds to the same form as in the original B3 model:

$$J_b(t,t') = q_1 + q_2 \int_{t'}^{t} \frac{ns^{-m}}{s - t' + (s-t')^{1-n}} \,\mathrm{d}s + q_3 \ln\left[1 + (t-t')^n\right] + q_4 \ln \frac{t}{t'} \tag{3.58}$$

where t and t' are expressed in days, $n = 0.1$ and $m = 0.5$ are fixed exponents and q_1, q_2, q_3, q_4 are material parameters. These parameters are estimated based on the concrete composition and compressive cylinder strength at 28 days in accordance to the B3 model:

$$q_1 = 126.77\ f_\mathrm{c}^{-0.5} \qquad [10^{-6}/\mathrm{MPa}] \tag{3.59}$$

$$q_2 = 185.4\ c^{0.5} f_\mathrm{c}^{-0.9} \qquad [10^{-6}/\mathrm{MPa}] \tag{3.60}$$

$$q_3 = 0.29\ (w/c)^4 q_2 \qquad [10^{-6}/\mathrm{MPa}] \tag{3.61}$$

$$q_4 = 20.3\ (a/c)^{-0.7} \qquad [10^{-6}/\mathrm{MPa}] \tag{3.62}$$

where:

c	is the cement content	[kg/m^3]
w	is the water content	[kg/m^3]
a	is the aggregate content	[kg/m^3]

The first term in the creep compliance function (3.58) represents the spring in Figure 3.3 with the asymptotic modulus $E_0 = 1/q_1$. The second and third terms represent the solidifying Kelvin chain and the fourth term represents a dashpot with age-dependent viscosity [18].

In the case of original B3 model, the viscosity of the ageing dashpot part is explicitly dependent on time according to:

$$\eta(t) = \frac{t}{q_4} \tag{3.63}$$

The microprestress theory explains the extremely high stresses at the microstructure scale caused by localised volume changes in the cement paste during the early stages of hydration. These volume changes are crucial for understanding the material's behaviour at early ages. The modification of the MPS theory by Jirásek and Havlásek leads to a reformulation of microprestress in terms of viscosity. In this updated version, a parameter representing the fluidity of the material, denoted as

μ_{S}, is introduced. Fluidity is the reciprocal of viscosity. This modification improves the incorporation of temperature and humidity dependencies. Thus, the viscosity is described by the first-order differential equation:

$$\dot{\eta} + \frac{\mu_{\text{S}}}{T_0} \left| T\frac{\dot{h}}{h} - k_{\text{T}}\dot{T} \right| (\mu_{\text{S}}\eta)^{p/(p-1)} = \frac{\psi_{\text{S}}}{q_4} \tag{3.64}$$

The initial viscosity is considered according to the equation (3.63). In the case where the exponent p is changed from the default value $p = 2$, it is possible to rewrite the equation (3.64) to the form:

$$\dot{\eta_f} + \frac{k_3}{T_0} \left| T\frac{\dot{h}}{h} - k_{\text{T}}\dot{T} \right| \eta_f^{\tilde{p}} = \frac{\psi_{\text{S}}}{q_4} \tag{3.65}$$

where:

$$\tilde{p} = p/(p-1) \tag{3.66}$$

$$k_3 = \mu_{\text{S}}^{\frac{1}{p-1}} \tag{3.67}$$

The second term on the left side (3.64), (3.65) reflects the influence of humidity and temperature. When neglecting the influence of humidity, respectively assuming constant humidity yields to:

$$\dot{\eta_f} + \frac{k_3}{T_0} \left| k_{\text{T}}\dot{T} \right| \eta_f^{\tilde{p}} = \frac{\psi_{\text{S}}}{q_4} \tag{3.68}$$

The value of coefficient k_{T} specifies microprestress generated by temperature increase. It distinguishes between monotonic k_{Tm} and cyclic k_{Tc} loading, thus it assumes that the microprestress evolves lower for the already exhibited temperature history [18].

To consider autogenous shrinkage, two implemented options are possible in OOFEM. The autogenous shrinkage can be determined in accordance with *fib* MC 2010 [15] or by the model B4. According to the model B4 the autogenous shrinkage for normal and slow-hardening cements develops:

$$\varepsilon_{\text{au,B4}}(t_e) = \varepsilon_{\text{au,B4}}^{\infty} \left[1 + \left(\frac{\tau_{\text{au}}}{t_e} \right)^{\frac{w/c}{0.38}} \right]^{-4.5} \tag{3.69}$$

where the autogenous shrinkage at infinity $\varepsilon_{\text{au,B4}}^{\infty}$ for normal cements equals to:

$$\varepsilon_{\text{au,B4}}^{\infty} = -210 \cdot 10^{-6} \left(\frac{a/c}{6} \right)^{-0.75} \left(\frac{w/c}{0.38} \right)^{-3.5} \tag{3.70}$$

and autogenous shrinkage halftime for normal and slow-hardening cements is:

$$\tau_{\text{au}} = 1 \left(\frac{w/c}{0.38} \right)^{3} \tag{3.71}$$

The rate of the thermal strain is expressed according to:

$$\dot{\varepsilon_{\text{T}}} = \alpha_{\text{T}}\dot{T} \tag{3.72}$$

3.3.4 Concrete fixed crack model

The *ConcreteFCM* model in OOFEM corresponds to the class of models commonly referred to in the literature as the smeared cracking approach [8], where the cracking strain is distributed over the finite element rather than being localised to discrete physical geometry. The term fixed crack indicates that crack initiates in the Gauss point and follows the maximum principal direction. This direction is maintained during crack propagation. As a consequence of different crack direction, shear stresses are present at crack surface. Comparably, the rotated crack approach assumes the propagation of crack in the direction of maximum principal stress. [21]

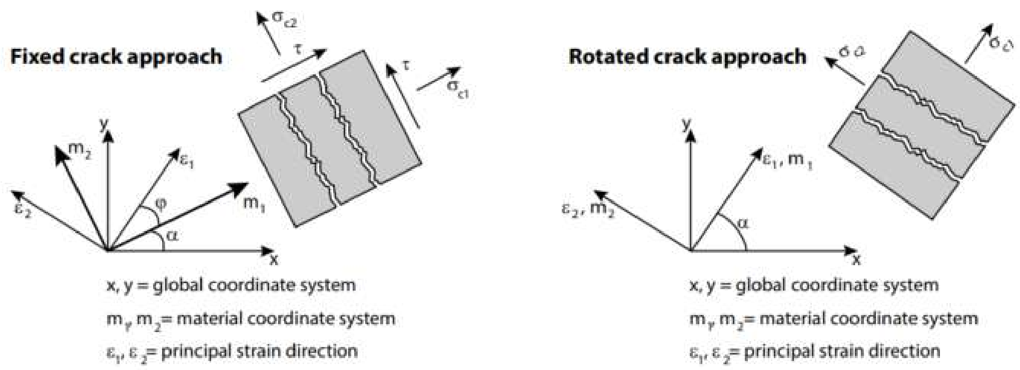

Figure 3.4: Fixed and rotated crack approach [39], reproduced by Malm [21]

The fixed crack model describes the tensile failure behaviour of concrete once the tensile strength is exceeded [26; 21; 39]. To ensure that energy dissipates correctly during fracture, the model uses the crack band approach, which links the softening behaviour with the size of elements [8]. For the post-peak softening, which describes the relation between the tensile stress and strain (crack opening), different descending branches are implemented in OOFEM. The simplest is linear softening, but for this analysis, the exponential descending branch has been chosen to better capture the crack-propagation behaviour. It is possible to incorporate other types of descending branch such as improved exponential Hordijk.

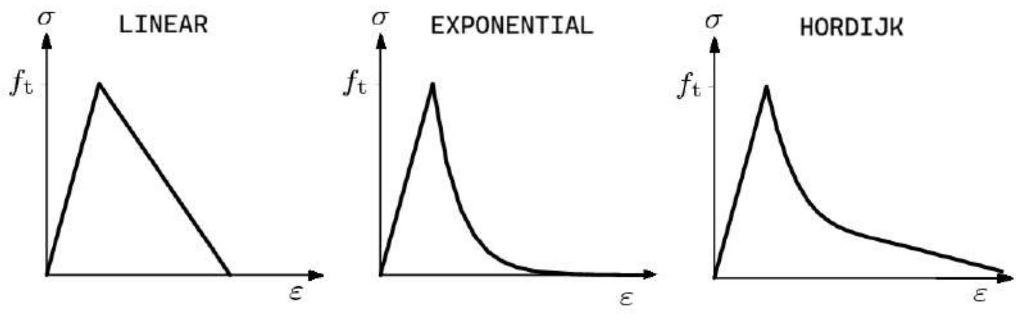

Figure 3.5: Stress-strain diagram for different softening models

The fracture energy G_f should ideally be determined from the experimental data, as it represents a material property. Because experimental data for fracture energy were not determined, it is estimated with the empirical formulae based on the mean compressive strength at 28 days according to *fib* MC 2010:

$$G_{\mathrm{f,28}} = 73(f_{\mathrm{cm,28}})^{0.18} \tag{3.73}$$

The time-evolution of fracture energy is assumed to be proportional to the time-dependence of tensile strength, as expressed by the following [26]:

$$G_{\mathrm{f}}(t) = G_{\mathrm{f,28}} \cdot \frac{f_{\mathrm{tm}}(t)}{f_{\mathrm{tm}}(28)} \tag{3.74}$$

The cracks for regular-strength concretes propagate within the transition zone of the aggregate and cement paste. Consequently, the crack surface is irregular with aggregate. As the aggregate from opposite sides touches within the crack it provides slight resistance to shear deformations [21]. As the crack width increase, the shear strength lowers. It is possible to take this effect into account by reducing the shear modulus [21].

3.4 Analysis and material summary

To accurately capture the interaction between thermal and mechanical behaviour, it is essential to describe the coupling of the analysis. In this analysis, the problem is solved using *StaggeredProblem* approach. Within this framework, the results of the thermal analysis, referred to as *prob1*, are exported and subsequently used as the input thermal field for the structural analysis, denoted as *prob2*. This refers to multiphysics integration framework that enables the coupling of different physical, such as thermal and structural analysis, through a staggered scheme.

A critical aspect of this coupling lies in the consistency of time-step setting across both sub-models, which ensures the stability and accuracy of the numerical solution. There are two primary approaches to address this issue. The first involves defining the time stepping exclusively within one of the submodels (typically the thermal model), whereby the time-step configuration of the structural model is disregarded. The second method specifies the time-step setting directly in the input file of the StaggeredProblem, which facilitates control of time discretisation. Moreover, this approach allows for adaptive time-stepping based on the convergence behaviour of the numerical iterations, enhancing computational efficiency.

Another important requirement is the consistency of geometry between the coupled sub-models. Although the overall geometry must remain compatible, the mesh resolution can differ between the thermal and structural analyses. When a coarser mesh is adopted for the thermal model, interpolation of the temperature field becomes necessary for use in the structural analysis. Note that for relatively uniform temperature fields, the interpolation error is negligible. However, in the case of highly nonlinear thermal gradients, such errors may become significant.

Furthermore, the structural model may be extended or simplified. In this case, it is extended to include the influence of reinforcement. In contrast, the influence of the sublayer is simplified.

For thermal analysis the concrete is assumed as *HydratingConcreteMat* with the affinity approximation of hydration process. The parameters of the model were calibrated based on the previously conducted experiments of isothermal calorimetry.

In the structural analysis, the incorporation of two material models results in a slightly altered mechanical response compared to the original models. When *ConcreteFCM* is coupled with the Microprestress–Solidification model *MPS*, the uncracked concrete is not represented as a linear elastic material but as an ageing viscoelastic. Consequently, the behaviour of the tensile fracture is connected to series with the MPS model, allowing the time-dependent response of the concrete to influence the fracture development, see Figure 3.6.

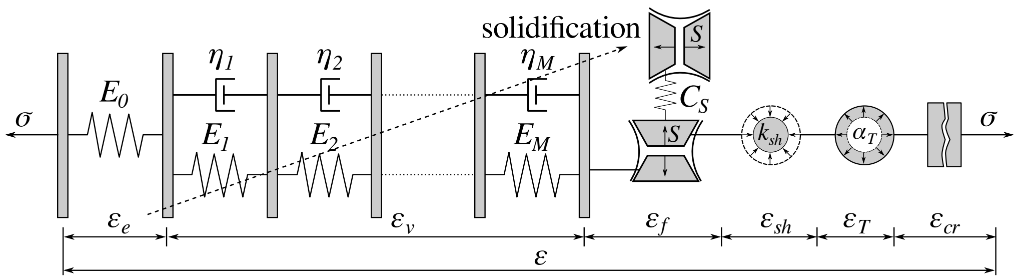

Figure 3.6: Rheological scheme of the MPS model connected with fixed crack model, provided by V. Šmilauer

Also the *MPS* model behaviour differs from original. In this case the moisture transfer have not been modelled, thus the effect of drying shrinkage and drying creep are not considered in the analysis. It accounts for the strain caused by basic creep, autogenous shrinkage and temperature. The basic creep, respectively microprestress is influenced by the varying temperature at the material points during the analysis.

Chapter 4

Polder Krounka

The construction of large hydraulic engineering structures, such as dams, is rare in the Czech Republic. One of the main reasons is the country's geomorphological and hydrological conditions, along with an already sufficient number of water reservoirs. However, due to contemporary climate change, the need for such structures is increasing, and their construction will likely rise in the coming decades.

One key reason for this development is the need to ensure an adequate water supply during dry periods. This concern led to the identification and protection of potential dam reservoir sites by the Ministry of Agriculture and the Ministry of the Environment in 2011. Another equally important reason is the increasing frequency of floods, making flood prevention a critical issue. In the case of the Krounka polder, the primary purpose is precisely that - mitigating the impact of rapid floods.

However, the preparation and construction of such projects can take years or even decades, not only due to the complexity of the project itself but also because of complicated property relations and public opinion. This was also the case for this project.

4.1 Location and regional context

The need for a flood prevention structure arose after the devastating floods in July 1997, which caused significant material damage in the Novohradka and Krounka river basins [28]. The most critical situation occurred in municipalities located downstream of the Krounka's confluence, such as Luže and Lozice, see Figure 4.1. In response, the state organization responsible for managing the Elbe River basin (*Povodí Labe, státní organizace*), which oversees both rivers, initiated a flood prevention programme for the region. As part of this initiative, potential dam locations were identified. The most appropriate location resulted in the contemporary construction place, see "Point 1" in Figure 4.1. The red line on the map indicates the Krounka River.

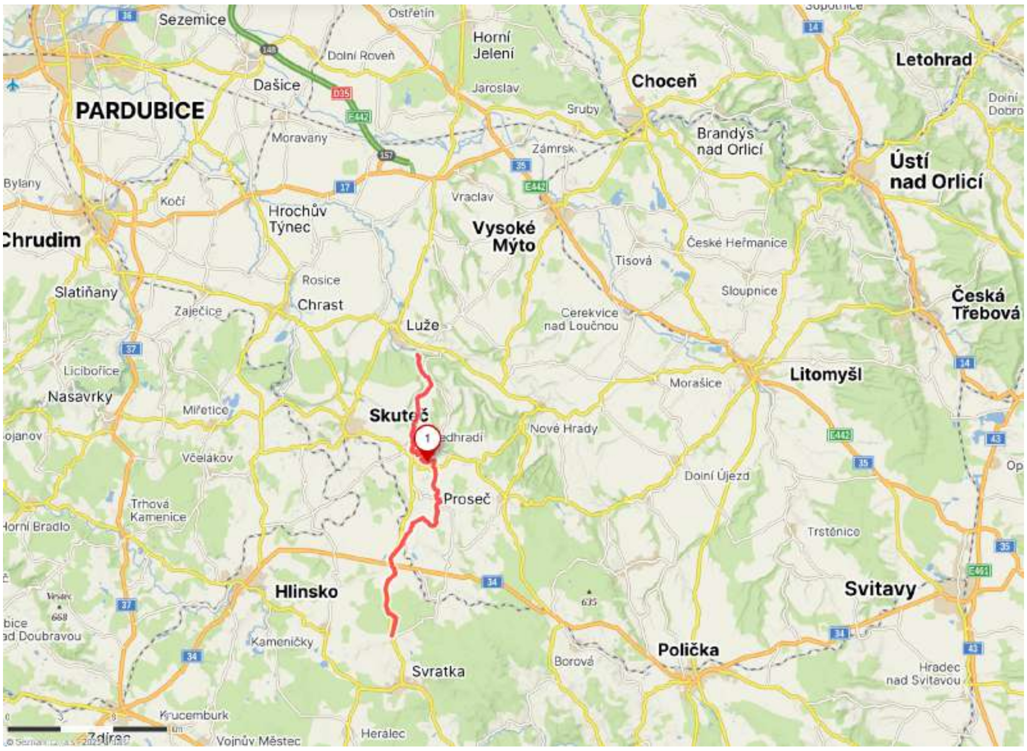

Figure 4.1: Construction location and regional context, source mapy.cz

The first phase of the programme involved the construction of flood barrier walls in the lower part of the Novohradka. However, the floods in 2006 showed that these measures were not enough. Consequently, efforts have been made to strengthen flood protection in the middle and upper sections of the Novohradka and Krounka rivers. Preparation of the construction began in 2010 but was stopped in 2012 due to issues related to private property ownership. [28]

The project was later revived following changes in the territorial development plan of the Pardubice Region "*Zásady územního rozvoje Pardubického kraje*", which designated the construction as a project of public benefit [28]. According to the Czech law in the case of publicly beneficial projects land and property expropriation is possible. Then the opposition from local residents soon emerged. In 2014, the inhabitants of a local municipal district formed the public organization Kutřín 42 in protest against the construction. The number represents the residents in the municipality at the time of the organization's formation [23]. The construction of this polder is a key component of the Flood Prevention Program III. [28]

The importance of this structure is highlighted by the recent floods in the beginning of September 2024, when the Novohradka overreached its channel due to the long heavy rains and caused damage in municipalities Luže and Lozice. This recent flooding is comparable with the floods in 1997 and 2006. The main idea of the polder is to prevent the flooding by capturing water in the reservoir. In this case the discharge of the Krounka and the Novohradka at confluence is very similar, therefore the idea to minimise the discharge of the Krounka at the confluence is effective. Thus, the construction lowers water level downstream and makes the already constructed flood barrier walls more effective.

The construction site is located near the municipality of Kutřín, just below the confluence of Martinice Stream (*Martinický potok*). In this area, the terrain transforms from flat land to a narrow and deep valley. Thus, it creates suitable conditions for the construction of the polder. However, the site is located on the edge of the natural park (*Přírodní park Údolí Krounky a Novohradky*), a protected area intended to preserve the authentic character of the landscape and valuable natural species. The border lines of the park are illustrated in Figure 4.2. The design of the polder takes these environmental considerations into account, aiming to minimise ecological impact while maximising flood protection for downstream areas. The area is closely linked to human activities. To give an example, a stone quarry is located nearby, see "Point 2" in the Figure 4.2.

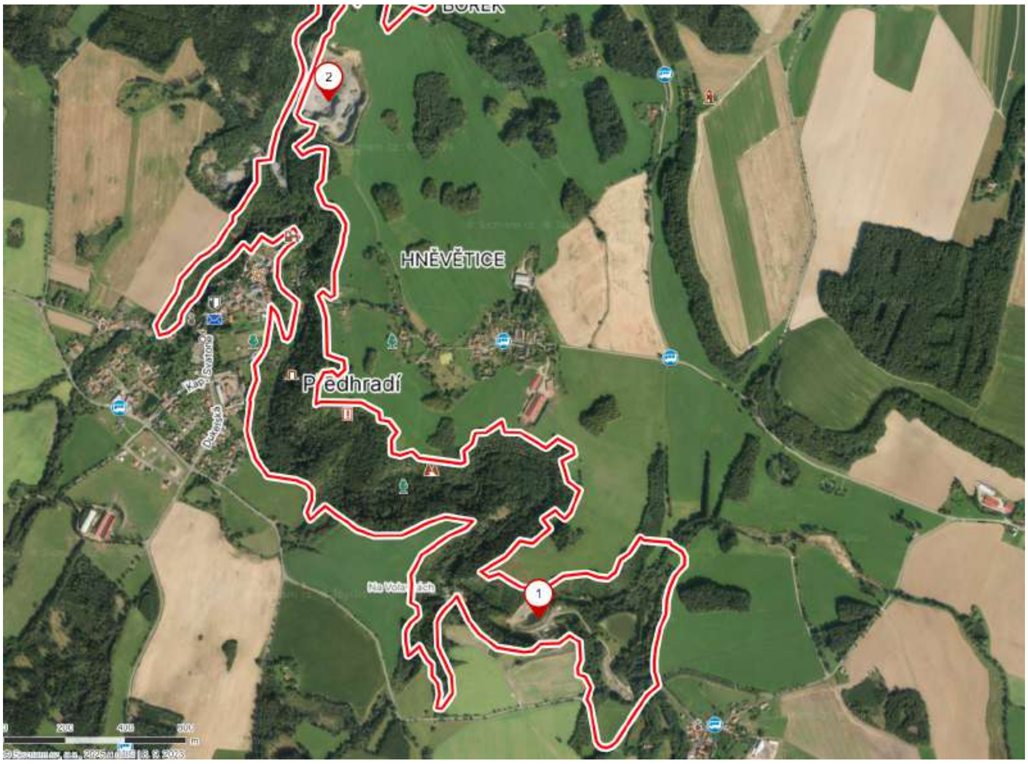

Figure 4.2: Detailed location, source mapy.cz

The reservoir has a maximum retention capacity of approximately 3.65 m^3 during a Q_{100} flood event. At full capacity, the inundated area will cover approximately 68 hectares, consisting mainly of pastures and forests. As part of the construction process, four residential buildings and a summer camp were relocated within the floodplain. [28]

4.2 Geometry and construction description

The primary structure of the polder is designed as a gravity concrete dam, which is covered with earth fill on both the upstream and downstream sides, hiding a vast part of the concrete structure. Special attention has been paid to the aesthetic integration of the dam into the significant landscape of the valley, see Figure 4.3. The visual design ensures a smooth transition between the dam structure and the surrounding rock outcrops and scree slopes. The connection of the polder to the slopes of the valley will be made by rock terraces, creating an illusion of the natural scree slopes.

Figure 4.3: Visualization of the polder Krounka, source Tender documentation [40]

The polder is 133.6 m long, 17.8 m high above the terrain, and has a crest width of 5.67 m. A reinforced roadway is planned along the crest. The dam is equipped with two bottom outlets and a migration passage. Under normal flow conditions, the main bottom outlet will remain fully open. It is designed to allow for the migration of fish and the passage of sediment. The outlet profile consists of a flowing channel at the bottom and dry berms on the sides to facilitate the movement of terrestrial species.

The cross-section of the dam body consists of a monolithic reinforced concrete structure in the shape of an “L”, composed of a foundation slab and an upstream wall. The upstream section ensures water tightness and frost resistance, as well as protection of the inner stabilising part of the dam from external environmental impacts. The foundation slab has a total height of 1.90 m and a width of 8.85 m at the foundation level. The vertical upstream wall has a maximum thickness of 3.055 m at its base and gradually lowers to 0.80 m at the crest, which gives the slope ratio 20:1 from the both sides of the upstream wall.

In the longitudinal direction, the dam is divided into a nine expansion parts with maximum length of 15 m. Furthermore, each expansion part is divided to the

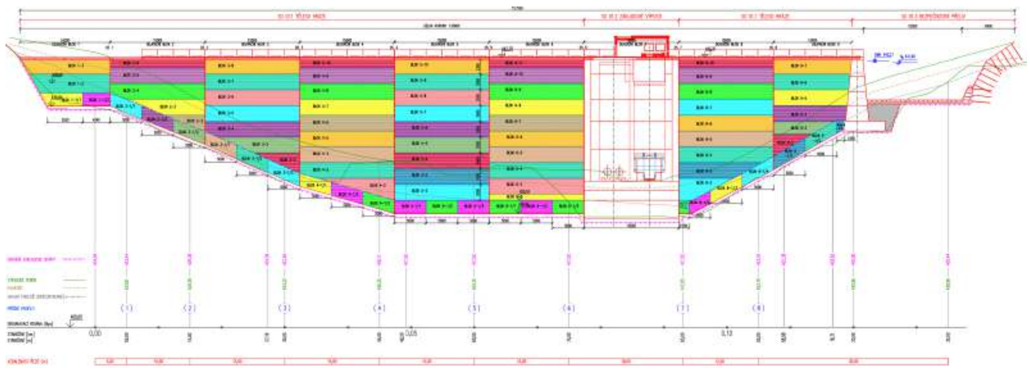

Figure 4.4: Structure blocks casting scheme, source Tender documentation [40]

separate blocks by height, see Figure 4.4. The increment height is set at 2.50 m, considering technological feasibility. The largest block of the upstream face has dimensions of 15×2.5×3.1 metres (length×height×width).

4.3 Pilot block

The pilot block for concrete casting is located within expansion part 7, in the upstream section before the inspection corridor, see Figure 4.5. The test block is placed on a prepared concrete base layer, thus its external movement is not restricted. The test block has the same parameters as the largest block of the upstream face, measuring 15×2.5×3.1 metres.

Figure 4.5: Pilot block position in the expansion part 7, source Tender documentation [40]

The main purpose of the pilot block is to verify the thermo-mechanical behaviour of the structure using proposed concrete mixture. A key focus of this verification is the formation of cracks, which is a critical factor in this project and requires special interest. Additionally, the pilot block provides valuable data for the computational model, enabling predictions of the behaviour of other sections of the concrete structure. The pilot block also serves to practise different parts of the construction process:

- Formwork composition
- Reinforcement installation
- Concrete placement technique
- Concrete curing method, including the water cooling system
- Positioning of sealing and drainage elements
- Examination of texture matrices for architecture concrete

4.3.1 Concrete

A key focus of this project was finding the right concrete mixture to reduce the risk of cracking. The last large concrete dam built in the area of the Czech Republic is Hněvkovice. This structure was built in 1991, more than 30 years ago. Since then, European standards for concrete and cement have been introduced, significantly changing construction practice. Thus, a careful study of new mixtures suitable for dam constructions was required.

Table 4.1: Concrete mixture specification

C25/30 (90d) - XC4, XF3, XA1 S4/S3 Dmax 22 mm		
Ingredient		**Quantity (kg/m^3)**
Cement	CEM II/B-S 32.5 R Mokrá	300
Fly ash	Opatovice	70
Water Content		
Effective water content		158
Absorption		15
Aggregate		
Fine aggregate	DTK 0/4 Čeperka	805
Coarse aggregate	HDK 8/16 Pohled	460
Coarse aggregate	HDK 11/22 Pohled	460
Additives		
Superplasticizer		1.4
Plasticizer		1.8
Air entraining agent		0.6
Total		2272

Because of described changes, research on potential concrete mixtures began in 2019. A key challenge was to prove satisfaction of the current requirements for mechanical and durability properties with a lower cement content compared to the contemporary minimum requirements. Thus, extensive testing of concrete mixture specimens was time-consuming. Nevertheless, two concrete mixtures had been proposed in 2020 [42]. The final concrete mixture recipe has been slightly modified by the concrete plant compared to the earlier proposed. Final concrete recipe is presented in the Table 4.1, however not all of the additives and its name are mentioned because of the proprietary knowledge.

To ensure the water tightness, the crack width is limited to 0.2 mm and maximum depth of 45 mm. The concrete satisfies the strength requirements of C25/30 in 90 days and meet the requirements for thawing and exposure classes of XC4, XF3 and XA1. Water cement ratio according to the concrete plant specification is 0.49, this value was calculated following EN 206+A2. Furthermore, the requirement for the maximum released hydration heat within 7 days with ambient temperature of 20 °C was set to 91 MJ/m^3. The maximum temperature of fresh concrete is limited with 27 °C, maximum temperature of the core part should not overreach 55 °C and maximum difference between the core part and the ambient temperature is allowed up to 20 °C. The requirements for maximum casting temperature and maximum temperature of the core part do not have to be satisfied when using the water cooling system.

4.3.2 Reinforcement

The reinforcement used for the pilot block is identical to that used in the upstream wall. The reinforcement type is of class B500B. Rebars in longitudinal direction consist of ∅25 mm and the transverse construction rebars of ∅16 mm. The surface reinforcement consist of ∅25 mm with the spacing of 150 mm, see Figure 4.6. The reinforcement ratio is approximately 0.6 % [41].

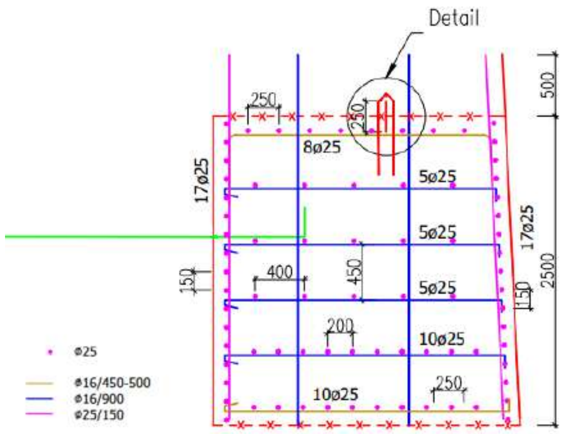

Figure 4.6: Typical reinforcement cross-section, source Tender documentation [40]

4.3.3 Water cooling system and monitoring setup

Even though the hydration heat was kept low by the design of the concrete mix, achieved through a lower cement content and partial replacement with fly ash, it was further reduced by an embedded water pipe cooling system. Due to the local availability of river water, the technique employed did not cause significant challenges. To ensure the operation of the system, an external water source from the wells and a cooling station were available at the construction site.

The cooling system is arranged in a 3×3 pipe layout, with the middle row aligned along the cross-sectional axis of symmetry. The pipe cooling system is illustrated in 3D model, see Figure 4.7. The pipes have an outer diameter of 25 mm and a wall thickness of 2.3 mm. The pipes are made of PE100, a high-density polyethylene (HDPE) material with a thermal conductivity of 0.43 W/mK, as specified by the manufacturer. These pipes meet the requirements for drinking water supply and could withstand temperatures up to 60 °C.

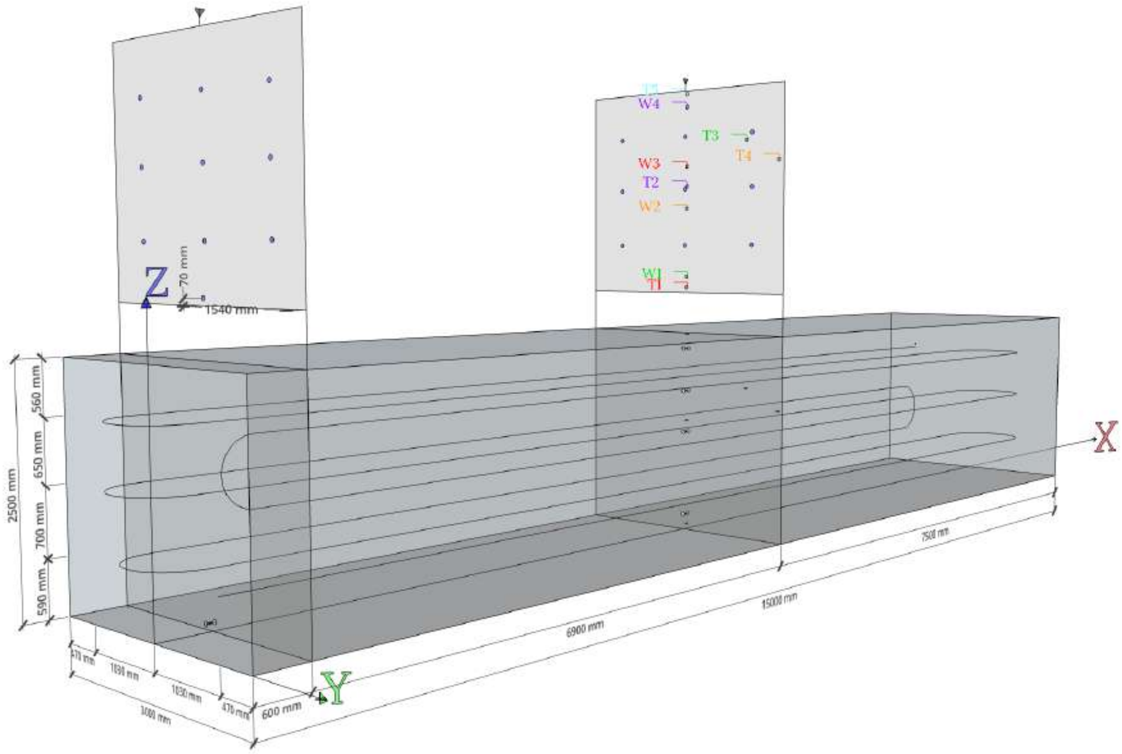

Figure 4.7: Block instrumentation (cooling pipe system and sensors)

In total, eight temperature sensors and five strain gauges were mounted, see the sensor position in Figure 4.7 and Table 4.2 with precise location. The temperature sensors used for measurement are of the Pt1000 type. Temperature sensors were calibrated in cold water to ensure consistent temperature reading, to diminish the effect of different cable lengths. For deformation measurements wire strain gauges SISGEO 0VK4200VC00 were used. These gauges also contain NTC thermistor temperature sensors, which provide less precise temperature readings.

Table 4.2: Sensors position

Temperature Sensors				Strain Gauges			
Sensor	**X (mm)**	**Y (mm)**	**Z (mm)**	**Sensor**	**X (mm)**	**Y (mm)**	**Z (mm)**
T1	7500	30	70	W1	7500	30	200
T2	7500	30	1320	W2	7500	30	1250
T3	7500	950	1850	W3	7500	30	1770
T4	7500	1420	1600	W4	7500	30	2300
T5	7500	30	2480	W5	600	-40	70
T6	600	-40	70				

Sensors T1, T2 and T5 were installed together with the strain gauges W1, W2, W3 and W4 on a ladder-like structure made of M12 threaded rods and inserted from above to the middle cross-section of the block, see Figure 4.8c. To prevent a false temperature reading from connection with steel reinforcement, most of the temperature sensors were attached to plastic holders. Temperature sensors T3 and T4 were mounted to the reinforcement in this cross-section, see Figure 4.8a.

(a) Sensors T3 and T4

(b) Strain gauge W5

(c) Ladder with sensors

Figure 4.8: Pilot block instrumentation with sensors

The strain gauge W5 was installed 0.6 m from the front side of the block, see Figure 4.8b. This gauge was installed to monitor the slip between the newly cast block and the previously cast foundation. From this sensor also the temperature data were obtained, in the experiment setup, denoted as sensor T6.

Two temperature sensors monitored the water temperature at the input $T_{w,in}$ and the output $T_{w,out}$, see Figure 4.9. These sensors were attached to the outer surface of the cooling pipe and insulated to eliminate the effect of the environment, see Figure 4.10b.

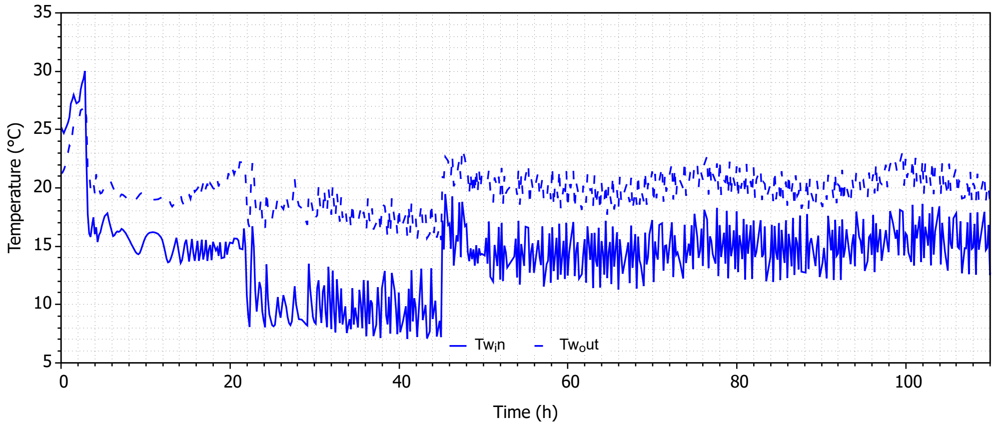

Figure 4.9: Water temperature on input and output

Last temperature sensor $T_{a,log}$ was measuring the air temperature near the central unit. This sensor was positioned one meter above the crane's concrete foundation and was not shaded, see Figure 4.10a. Therefore, the results were influenced by the effect of sun radiation and were not used. The air temperature data were replaced with the data obtained from the meteorological station installed on the construction site.

(a) Central unit

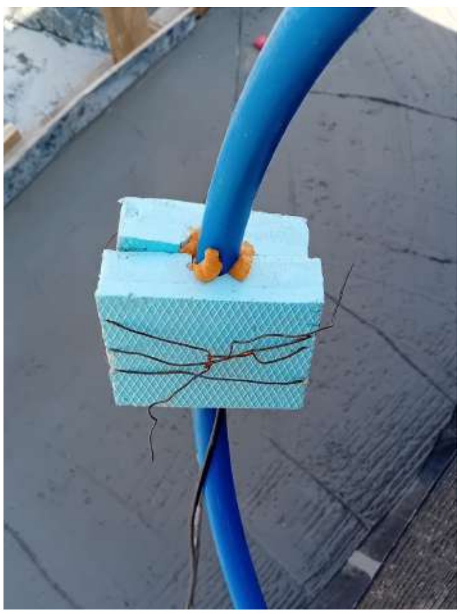

(b) Attached temperature sensor

Figure 4.10: Central unit and temperature sensor of cooling pipe

Data were recorded every 10 minutes using a DataTaker DT80g central unit and transmitted every 6 hours to an FTP server. A 40W photovoltaic panel was connected to ensure a stable power supply. Due to the risk of flooding in the construction site, the central unit was installed on the concrete foundation of the crane.

4.3.4 Casting and curing

The construction of the pilot block was cast on 6$^{\text{th}}$ August 2024, see Figure 4.11. The pilot block casting started at 8:30 and ended at 14:15. The temperature of the fresh concrete was within 21.4 and 28.8 °C. During the casting, specimens were taken for the laboratory measurement of shrinkage (autogenous and drying) and basic creep. The cooling system was turned on immediately after the casting had finished.

Figure 4.11: Pilot block casting, photo provided by P. Reiterman

The insulation of 40 mm XPS boards were put to the formwork. According to the results and site picture, the thickness of the front and back insulation was probably lower 30 or 20 mm of XPS. The top surface was sealed with a plastic foil and covered by 4 layers of three-milimeter-thick geotextile. The project assumed with a minimal curing period of nine days. In reality the formwork was removed on 26$^{\text{th}}$ August, eleven days after casting, see Figure 4.12. The cooling system was switched off on 11$^{\text{th}}$ August.

Figure 4.12: Cast block after formwork removal, photo provided by P. Reiterman

4.4 Thermo-mechanical analysis

As previously mentioned, the suitable choice supporting the connection between thermal and mechanical analysis is OOFEM. While the main FE calculations are run in OOFEM, the geometry and object mesh are defined in the French CAD program Salome, and results such as stress fields, crack propagation, and temperature distribution are visualised and analysed using ParaView. Furthermore, in this part details connected to the analysis of the pilot block are presented and discussed.

4.4.1 Model geometry and FE discretization

When the slight inclination of the side is neglected, two axes of symmetry can be assumed. However, only the longitudinal symmetry axis is considered to ensure that potential crack propagation can occur at the midpoint of the cross-section. For structural components, such as reinforcement rebars or cooling pipes, positioned along the longitudinal axis of symmetry, it is necessary to adjust their property specifications. The main model dimensions are 1.5(w/2)×2.5(h)×15(l) m.

For thermal analysis, the previously cast base concrete is also included in the model, see Figure 4.13a. However, for mechanical analysis, it is sufficient to exclude this part to reduce computational complexity. Instead, a layer with a thickness of approximately 200 mm is assumed.

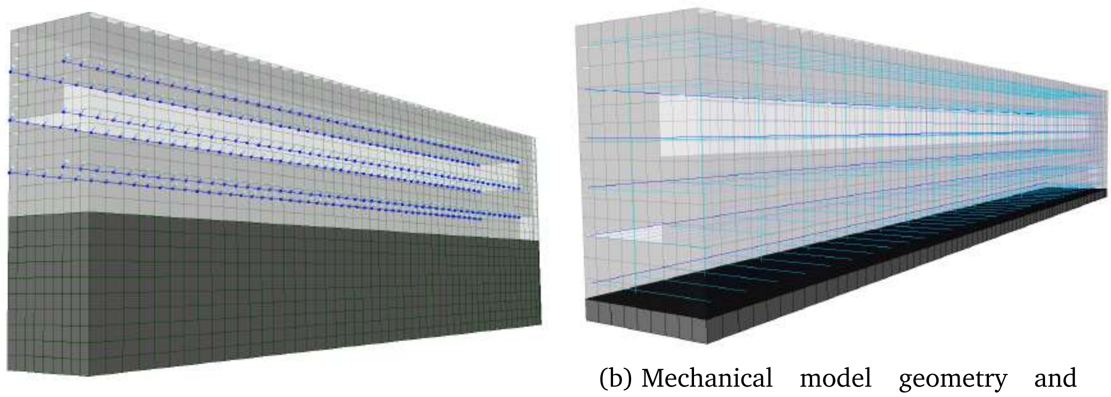

(a) Thermal model geometry and mesh

(b) Mechanical model geometry and mesh

Figure 4.13: Geometry and mesh for the analysis

First, a plane mesh was created with strictly defined nodes corresponding to the positions of the cooling pipes. The remaining areas were meshed with a maximum element size limit of 200 mm. Although this may seem like a relatively coarse division, the thermal field still corresponds well to reality, except for minor discrepancies near the cooling pipes at early ages. The mesh was then expanded into a 3D model by specifying the third dimension with length of 300 mm.

Instead of directly modelling the fracture process zone with actual width w_c, an element-wide crack band of width h with the same size as the mesh is assumed. According to the crack band theory for concrete proposed by Bažant [8], it is essential to ensure that correct value of the fracture energy is preserved. In other words, the work of the surrounding structure on the fracture process zone is equal to the dissipated energy. Consequently, this ensures the size bias and numerical instability are eliminated by the appropriate selection of the mesh size. According to Bažant [8], appropriate maximum size of the finite mesh is **a half** of:

$$h < \frac{2G_f E}{f_t^2} \tag{4.1}$$

where:

G_f	is fracture energy,
E	is Young's modulus of elasticity
f_t	is tensile strength

It is important to note that all three of the aforementioned parameters are time-dependent. As the properties are described by different time functions, the maximum mesh size may change during the analysis. To ensure accuracy and stability, it is essential to satisfy this criterion. Therefore, a conservative mesh size of 200 mm is chosen for the third dimension.

For solid concrete parts, eight-node isoparametric elements are used, see Figure 4.14. For the thermal analysis *Brick1ht* elements with one degree of freedom at each node are used and for mechanical analysis *LSpace* elements with three degrees of freedom at each node. By default, 8 integration points are necessary [25], however, 27 integration points increased accuracy.

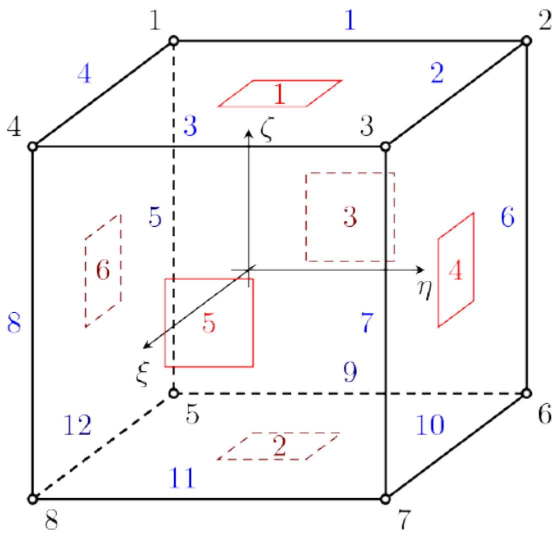

Figure 4.14: Eight-node brick element[25]

The cooling pipe system is not modelled directly. Instead the nodes at the location of the cooling pipes are connected through a truss member *Line1ht* to a fictive node. The temperature is directly specified at these nodes by the Dirichlet boundary condition and the truss element describes the pipe within the side of brick element h. Thus, the cross-sectional area A and thermal conductivity λ_{fic} are adjusted according to:

$$A = \pi h(d_0 - t) \tag{4.2}$$

$$\lambda_{\text{fic}} = \frac{\lambda_{\text{HDPE}} \cdot l_{\text{t}}}{t} \tag{4.3}$$

where:

d_0 is outer diameter of the cooling pipe,
t is the wall thickness of cooling pipe,
l_{t} is length of the truss element

When inserting the values to the Equation (4.3), it results to fictitious thermal conductivity λ_{fic} of 18.696 W/mK.

The reinforcement is modelled using *truss3D* elements, with three degrees of freedom at each node. Since reinforcement nodes do not naturally align with the original mesh, an effective approach is to use hanging nodes that do not introduce additional degrees of freedom. Instead of being independent, the displacements of the hanging nodes are interpolated from the surrounding mesh. This simplifies modelling, ensures compatibility for the deformation, and avoids a significant increase in computational cost.

4.4.2 Material specification

For thermal analysis, the properties of the pilot block concrete and the base concrete are assumed identically. The only difference is that the base concrete is considered as already matured and the hydration is not modelled. The hydration of the pilot block is assumed with the previously discussed *HydratingConcreteMat* with the parameters described in Table 3.2.

The density of the base concrete is assumed to be slightly higher compared to the pilot block. The specific heat is determined by weight average based on the concrete mixture composition and rounded up. The thermal conductivity determined by this method is roughly 2.5 W/mK and significantly differs compared to the conductivity values from previous simulations with similar concrete mixture [42; 41]. Thus, the thermal conductivity is chosen in relation to these results and assumed with value 1.50 W/mK to fit the experimental results.

The reason of the difference can be justified by the influence of air entering agent, which reduces the conductivity as the consequence of increased air-voids. The influence of the reinforcement for thermal analysis is neglected, but for the mechanical behaviour it is incorporated. In accordance with the truss element type, the characteristics in bending are not considered, only axial deformations are assumed.

As discussed previously, concrete is described as an ageing viscoelastic material with tensile fracture. Therefore, the Young modulus is adjusted to account for the vertical stiffness of the base concrete. For simplicity, it is assumed as linear isotropic elastic material. Steel reinforcement is assumed as elastic-plastic with von Mises yield criteria.

Parameters of the Microprestress-Solidification theory model *MPS* and fixed crack model *ConcreteFCM* are determined based on the concrete composition and laboratory tests if possible. Otherwise, the parameters are determined in accordance with European technical standards, design model codes and appropriate literature. The parameters k_3 and k_{Tm} are set in accordance with the experimental results of the dissertation thesis [16]. For detailed values of material properties, see Table 4.3.

Compressive strength of the concrete is determined based on the experimental cube tests conducted on 18 specimens at 90 days according to Eurocode EN 12390. The characteristic 28-day compressive strength results in 28.3 MPa when approximated to a time-dependent relation in Eurocode EN 1992-1-1. Based on this estimated characteristic compressive strength, the tensile strength is conservatively assumed following the code-based relationship. Thus, the mean tensile strength is $f_{\text{ctm}} = 2.8$ MPa. However, results from four-point flexural bending tests on three specimens indicate a higher tensile strength ($f_{\text{ctm,bending}} = 3.1$ MPa) than the assumed value. The comparison of compressive and tensile strength development for the assumed site mix (denoted as C28/36) and regular concrete C25/30 is graphically visualised, see Figure 4.15. Also note, that the comparison is for regular concrete mix with specified 28-day strength, in the project the concrete class strength is assumed in 90 days.

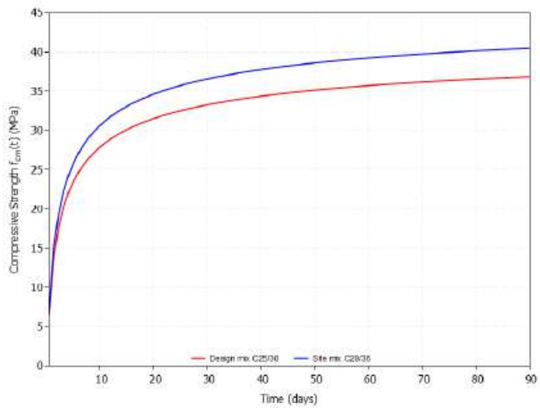

(a) Compressive strength development

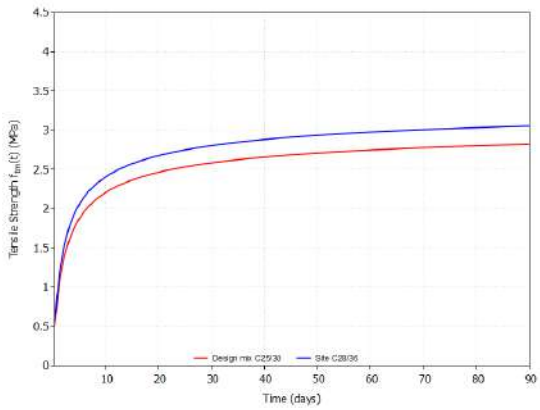

(b) Tensile strength development

Figure 4.15: Comparison between mix C25/30 and site mix C28/36 for compressive and tensile strength

The value of fracture energy is empirically determined based on *fib* MC 2010. Autogenous shrinkage at infinity is also chosen in accordance with laboratory measurements on specimens taken during pilot block casting.

Table 4.3: Material properties

Property	**Unit**	**Pilot Block** Concrete	Steel	**Base Concrete**
Thermal Properties				
Density ρ	kg/m^3	2275	-	2300
Thermal conductivity λ	W/mK	1.50	-	1.50
Specific heat c	J/kgK	940	-	940
Mechanical Properties				
Density ρ	kg/m^3	2275	7850	2300
Young's modulus E	GPa	-	200	1.5
Poisson's ratio	–	0.20	0.30	0.20
Thermal expansion coefficient	10^{-6}/K	10	10	10
Compressive strength f_{cm}	MPa	36.3	-	-
Tensile strength f_{tm}	MPa	2.8	-	-
Fracture energy G_f	N/m	139	-	-
Yield strength f_y	MPa	-	500	-
Cement content c	kg/m^3	300	-	-
Water cement ratio w/c	–	0.52	-	-
Aggregate cement ratio a/c	–	5.48	-	-
Parameter p	–	1000	-	-
Parameter k_3	–	90	-	-
Parameter k_{Tm}	–	0.2889	-	-
Infinity autogenous shrinkage	$\mu\varepsilon$	50	-	-

4.4.3 Initial and boundary conditions

The thermal analysis begins at the midpoint of the casting process, which is set to 11:22 on August 6$^{\text{th}}$, defining $t = 0$. The initial temperature of the concrete mixture is assumed to be the average of the measured range, resulting in 25.1 °C. The initial temperature of the base concrete was not measured or explicitly determined. It likely varies with depth, but for simplicity, a uniform temperature is assumed. Given the summer conditions, 20.0 °C is considered a reasonable estimate.

It is important to note that the boundary conditions mimic real conditions. To simplify the problem while maintaining a satisfactory level of accuracy, certain adjustments are made. The boundary conditions are defined in accordance with the corresponding timeline:

- Aug 6, 2024 11:22 $t = 0$ h:
  - Cooling pipe system is activated.
  - Heat exchange between insulated surfaces and the surroundings is described by the Newton boundary condition.
  - Heat exchange between the base concrete and the ground is modelled using the Newton boundary condition.
  - Solar radiation is considered for the top and side surfaces using the Neumann boundary condition.
- Aug 11, 2024 $t = 110$ h:
  - Cooling pipe system is deactivated.
- Aug 17, 2024 $t = 270$ h:
  - Heat exchange coefficient for the top and side surfaces is adjusted due to formwork removal.
  - Solar radiation on the side surfaces is updated to reflect formwork removal.

It is possible to fairly well approximate the ambient temperature $T_{\mathrm{a,met}}$ by the goniometric function series [10]. In this case, serie of three sinusoids had been employed. Approximation parameters were found with the script created in Python using SciPy's optimise module. Thus, the function of ambient temperature approximation follows:

$$\begin{aligned} T_{\mathrm{a,approx}}(h) = 5.507\sin\left(\frac{2\pi}{23.249}(t-16.543)\right) + 1.817\sin\left(\frac{2\pi}{128.742}(t+2.238)\right) \\ + 2.225\sin\left(\frac{2\pi}{400.432}(t-87.567)\right) + 20.1 \end{aligned} \tag{4.4}$$

The approximation can be compared with the original values, see Figure 4.16. The temperature measured by the sensor close to the crane $T_{\mathrm{a,log}}$ has only informational character and have not been used.

Other part of the Newton boundary condition is the heat transfer coefficient between the surface and the environment. Since the formwork and insulation layers are not explicitly modelled, their effect is taken into account when calculating the thermal resistance of each layer [10]. The total thermal resistance of all layers follows:

$$R_{\mathrm{s}} = \frac{1}{\beta} + \sum \frac{t_i}{\lambda_i} \tag{4.5}$$

where:

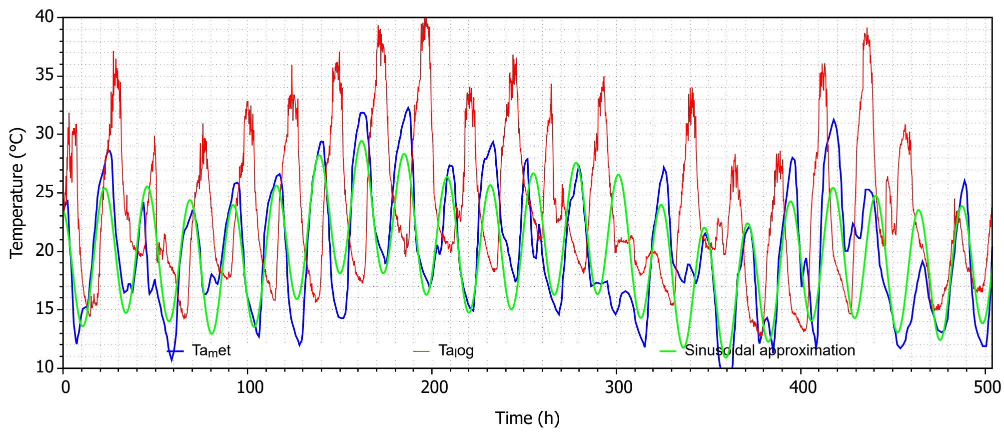

Figure 4.16: Comparison of measured air temperature and approximation

β is surface conductance,
t_i is the layer thickness,
λ_i is the layer thermal conductivity

The insulation layers have minimal thermal capacity and can be neglected, the equivalent surface conduction coefficient is given by:

$$a = \frac{1}{R_s} \tag{4.6}$$

The surface conductance β of solid in air depends on the wind speed and roughness of the surface. The approximate value can be assumed based on the wind class and formula proposed by Bofang [10] for smooth surface:

$$\beta = 18.46 + 13.60F^{1.36} \quad \text{kJ/(m}^2\text{h}\,^\circ\text{C)} \tag{4.7}$$

where:

F is the wind class

Wind class 1 has been assumed, with a wind speed in range of 0.3-1.5 m/s [10]. Thus, the surface conductance β calculated by Equation 4.7 equals to 8.905 W/m^{2}K. This value is also assumed as the thermal conduction coefficient for the pilot block surfaces after removal of the formwork. The coefficient of heat transfer within the base block and ground is $a_{\text{ground}} = 2.500$ W/m^{2}K.

In Table 4.4, a summary of layer compositions is provided, including their thickness, thermal conductivity, thermal resistance and equivalent coefficient of surface conduction for all assumed sides. The thermal conductivity values used are those commonly applied in civil engineering practice. However, the thermal conductivity of geotextiles is rarely found in standard reference tables and is not typically specified by the manufacturer. It has been observed that the thermal conductivity

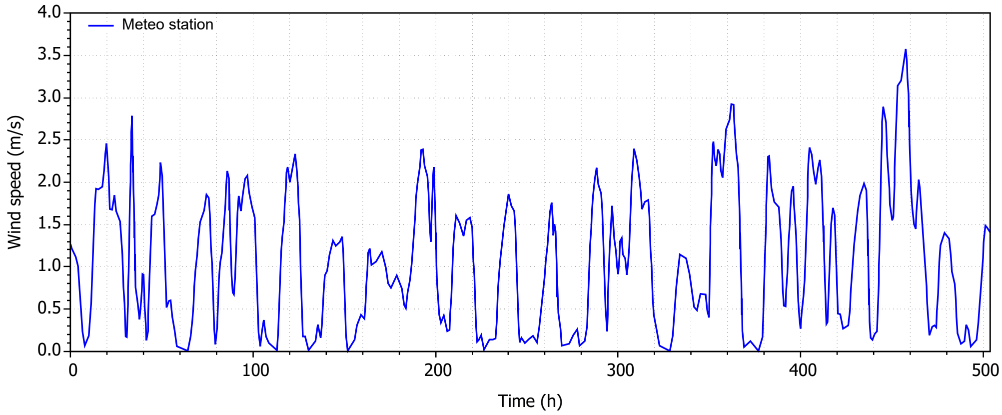

Figure 4.17: Measured wind speed

of geotextiles can vary significantly depending on the water content. When air voids are replaced by water, conductivity can increase up to 0.83 W/mK [33]. According to existing studies, the thermal conductivity of dry geotextiles ranges from 0.07 to 0.13 W/mK [33]. Therefore, for this purpose, the thermal conductivity of geotextile is assumed to be 0.1 W/mK.

Table 4.4: Thermal properties of side compositions

Specification **Material**	**Thickness** mm	**Conductivity** W/mK	**Resistance** m^2K/W	**Coefficient** α W/m^2K
Top Composition				
Foil PE	0.1	0.350	0.0003	-
Geotextile PP	15	0.100	0.1500	-
Surface/Air	-	-	0.1123	-
			0.2626	**3.808**
Side Composition				
Insulation XPS	40	0.035	1.1429	-
Plywood	21	0.130	0.1615	-
Surface/Air	-	-	0.1123	-
			1.4167	**0.706**
Front/Rear Composition				
Insulation XPS	20	0.035	0.5714	-
Plywood	21	0.130	0.1615	-
Surface/Air	-	-	0.1123	-
			0.8453	**1.183**

In the analysis, it was recognised that the effect of solar radiation needs to be considered. Factors such as summer casting and the deforested, open location of the site within the valley contribute to this effect, as evidenced by meteorological station data, see Figure 4.18.

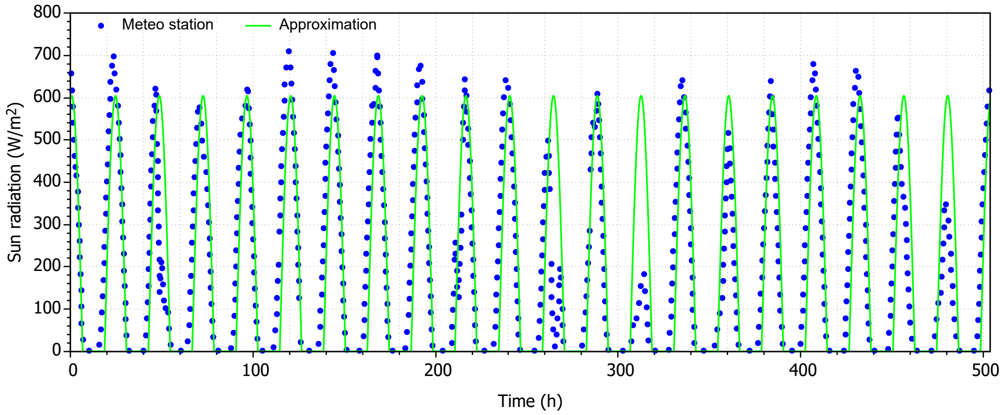

Figure 4.18: Comparison of measured sun radiation and approximation

For simplification, solar radiation is represented using a Newton boundary condition with a prescribed heat flux. The heat flux is modelled as a function based on the positive portion of a sinusoidal term, where a full cycle represents a 24-hour period. The positive section corresponds to the time interval between 6:00 am and 6:00 pm, with a peak occurring at noon. In addition, an adjustment is applied to account for the initial time shift. The sinusoidal term is scaled by the average value of the daily peaks $q_{\text{max,avg}}$. The approximation of the solar radiation, see Figure 4.18, is as follows:

$$\begin{aligned} q_{\text{radiation}}(t) &= q_{\text{max,avg}} \cdot \sin\left(\frac{2\pi}{24}(t+5.367)\right) \quad \wedge \quad q_{\text{radiation}}(t) \geq 0 \\ &= 604.5 \cdot \sin\left(\frac{2\pi}{24}(t+5.367)\right) \quad \wedge \quad q_{\text{radiation}}(t) \geq 0 \end{aligned} \tag{4.8}$$

It is important to note that, the absorb factor is considered with the value of 0.35. Moreover, in comparison to real conditions, the boundary conditions for solar radiation are directly applied to the concrete surface. In reality, the thermal effect is significantly influenced by the layer composition, leading to a lower impact on the concrete surface than on the top of the insulated layer. Consequently, the constant values were adjusted to reflect the surface composition and increased following its removal. The constants were estimated through a manual iteration process to best replicate the experimental data. Moreover, the increase in the insulation layer also introduced a shift in the solar radiation intervals. For the top surface, this shift is found to be negligible. However, for the side surface, it must be considered. In this case, the shift is caused by the combined effect of the cardinal orientation and the thickness of the insulation. As a result, the peak solar radiation on the side surface is observed to occur with a delay of approximately four hours.

For the mechanical analysis, the model is less constrained compared to the thermal analysis. Firstly, the nodes located at the longitudinal face of symmetry, along which the model is simplified, are restrained in the transverse (y-axis) direction. The restrain conditions of the base concrete are more complex. Therefore two different extreme scenarios are assumed. For both, the nodes on the bottom surface of the base concrete are restricted in the vertical (z-axis) direction. Both modelled cases assume the restrained movement in the longitudinal direction (x-axis) close to the mid-section of the block. First scenario modifies the vertical stiffness of the underlay to simulate the compressibility of the real base concrete. Thus, the Young modulus is reduced to 1.5 GPa, see Table 4.3. In the second case, the Young modulus is overestimated to 300 GPa to model very stiff conditions of the base. While conservative, this may not reflect the real-world conditions and can lead to overestimation.

Chapter 5

Results

This chapter presents the results of the finite element analysis and compares them directly with the available experimental data. The aim is to assess the accuracy of the numerical simulation and reproduce the observed behaviour. Structural and thermal responses are validated for locations of the sensors.

Where discrepancies between the FE model and experimental results are identified, possible explanations are carried out. These reflections consider modelling assumptions, material parameters, boundary conditions and numerical limitations. The findings serve not only to validate the model but also to provide insight into the sensitivity of the simulation to various influencing factors, which can serve as guidance for potential model refinement.

5.1 Validation of thermal model

To validate the results of the thermal analysis, the temperatures at mesh nodes located nearest to the installed thermocouples are extracted for comparison, see Figure 5.1. In most cases, the closest node is used directly. However, for the thermocouple T2, node No.2125 is selected instead of the geometrically closer node No.2075. Overall, the analysis temperatures align well with the experimental data, apart from several reported discrepancies. It shows that, when the hydration model parameters, initial and boundary conditions for thermal analysis are appropriately set with respect to the reality, it reaches well alignment with very low error.

For improved readability, the results are divided into two separate graphs, see Figure 5.2 and Figure 5.3. The experimental data are represented by markers, while the model predictions are shown as solid lines. It should be noted that, for clarity, the number of displayed experimental data points has been reduced compared to the full dataset obtained during field experiment. Nevertheless, the selected data provide a representative overview and allow a clear comparison between the numerical model and the experimental observations.

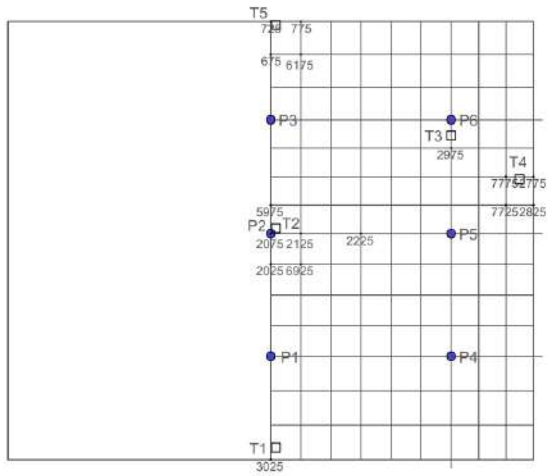

Figure 5.1: Alignment of mesh nodes with installed thermocouples (x=7.5 m)

The thermal sensor T1, located at the bottom of the mid-section, shows excellent agreement with the simulation results. The maximum deviation remains within 1 °C, indicating a high level of accuracy. The assumed initial temperature of the base concrete corresponds to the measured temperature of the fresh concrete mix. During hydration, the temperature rises to approximately 38 °C before gradually decreasing to around 30 °C. Around $t = 120$ h, a slight change in the slope of the temperature curve is observed, corresponding to the shutdown of the cooling pipe system. Additionally, the experimental data exhibit minor daily fluctuations between day and night, which are not captured by the simulation.

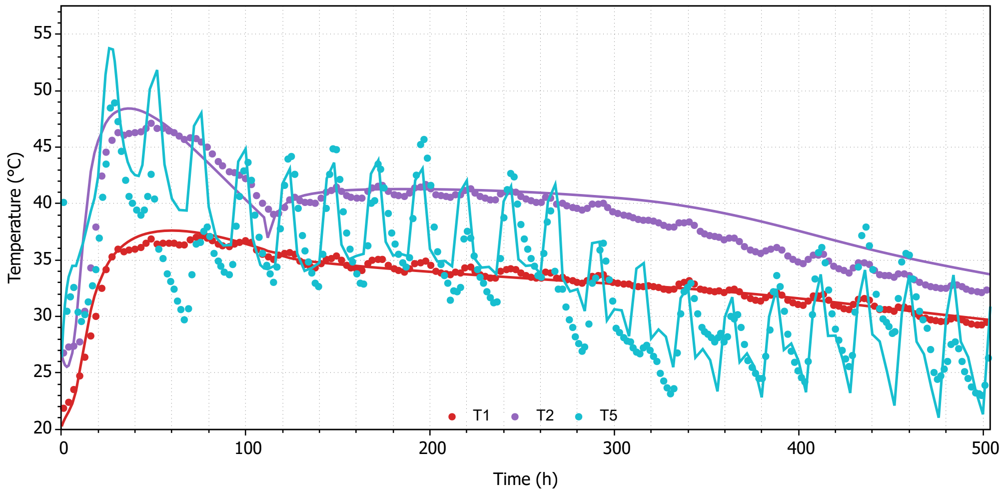

Figure 5.2: Comparison of numerical and experimental data for selected sensors (points - experiment, lines - model)

Sensor T6 is also installed at the bottom surface but positioned near the beginning of the block (at approximately $x = 0.6$ m). The simulation predicts a similar value for the maximum hydration temperature as observed for sensor T1. However, the measured temperature at this location does not exceed 35 °C, resulting in a maximum discrepancy of approximately 3 °C during the hydration peak. Furthermore, the simulation predicts a faster cooling rate compared to the experimental data, which may be attributed to the prescribed boundary condition on the front side of the base concrete.

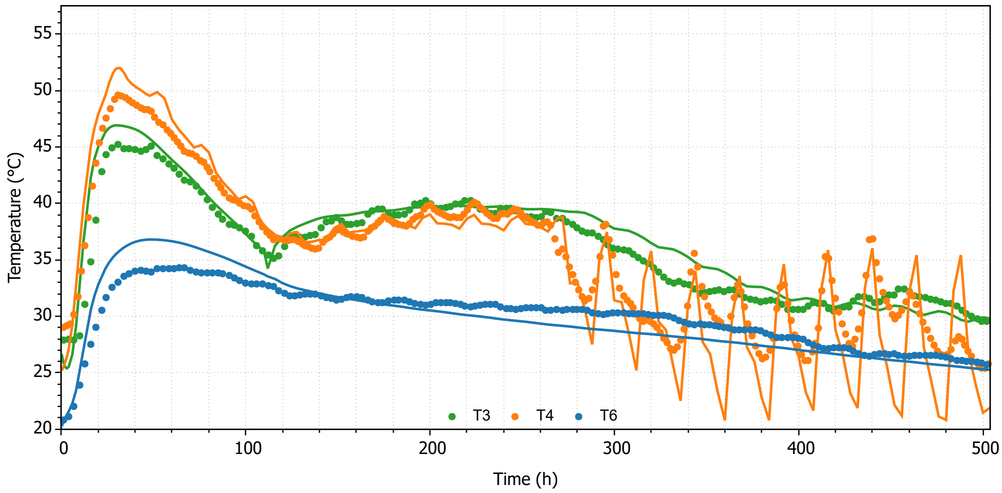

Figure 5.3: Comparison of numerical and experimental data for selected sensors (points - experiment, lines - model)

Sensors T2 and T3 exhibit very similar temperature profiles due to their placement near cooling pipes P2 and P6, respectively. The experimental data align well with the numerical simulation, although the model slightly overestimates the hydration peak temperatures by approximately 2 °C. During the active cooling phase provided by the installed pipe system, the concrete in the central region cools in reality more slowly than predicted by the simulation. Notably, the temperature drops to around 40 °C for sensor T2 and 35 °C for sensor T3 during cooling, followed by an increase once the system is turned off. After removal of the formwork (approximately at $t = 270$ h), the effect of solar radiation becomes apparent, particularly for sensor T3. In this case, the simulation slightly underpredicts the cooling observed experimentally, likely due to inaccuracies in the approximation of ambient temperature and solar radiation.

The numerical results for sensor T5 agree well with the measured data, except for the major error around 10 °C in the beginning of the analysis. The reason for this error comes from the assumed insulation cover of the top surface. At first, the top surface was only covered by one layer of the geotextile and later with several layers were added. Thus, the heat transfer coefficient for beginning times is higher than assumed in the analysis. Consequently, the measured temperatures are lower than numerically estimated. The results are influenced by the solar radiation and ambient temperature resulting in the daily temperature fluctuation around 10 °C. The alignment of the simulation with real data for this place is strongly dependent on the approximation of the ambient temperature and solar radiation.

The results of the numerical analysis for sensor T4 overall correspond well with the measured data. A temperature difference of approximately 5 °C is observed at the early stage, likely due to the different temperature of fresh concrete. After the removal of the insulated formwork, the simulation slightly underestimates the minimum daily temperature peaks. This discrepancy is attributed to the position of the reference point used in the simulation, see Figure 5.4. For node No.7775, the daily temperature fluctuation is less pronounced due to the thermal buffering effect of the surrounding concrete.

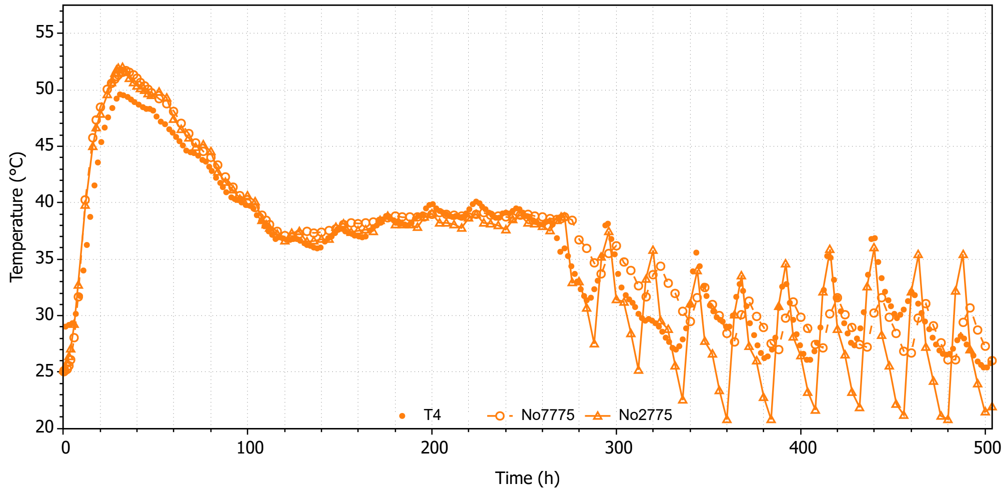

Figure 5.4: Comparison of temperature profile for nodes close to T4

The decision for selecting node No.2125 instead closer node No.2075 for the sensor T2 is made because node No.2075 is directly affected by the cooling pipe, which locally influences the temperature field. Furthermore, the theoretical alignment between the position of the cooling pipe and sensor T2 is discussable. It is important to note that the ladder with attached sensors was installed first and later cooling pipe system. It is very likely, that the cooling pipe is placed from the opposite side of the installed sensor. Thus, it is farther from the cooling pipe. It is possible to see this in Figure 5.5.

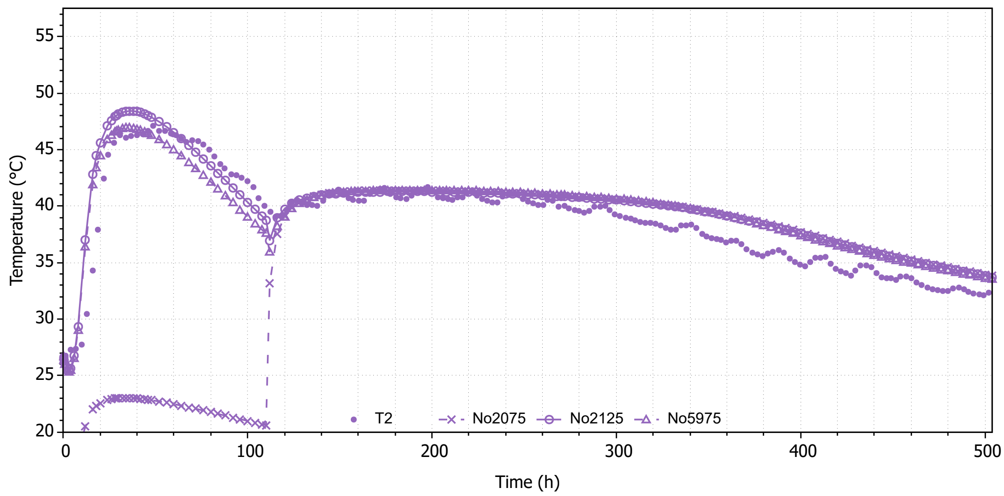

Figure 5.5: Comparison of temperature profile for nodes close to T2

5.2 Extension of thermal analysis

The node No.2225 and No.2075 are selected to monitor the maximum temperature of the block during analysis. During the active cooling the maximum temperature of 55 °C is reached after 40 h from the assumed beginning. When the pipe cooling system is turned off the temperature increases in the central part of the cross-section, resulting in slightly higher temperature for the node No.2075, which is closer to the cooling pipe P2. As seen in the Figure 5.6 the difference is negligible.

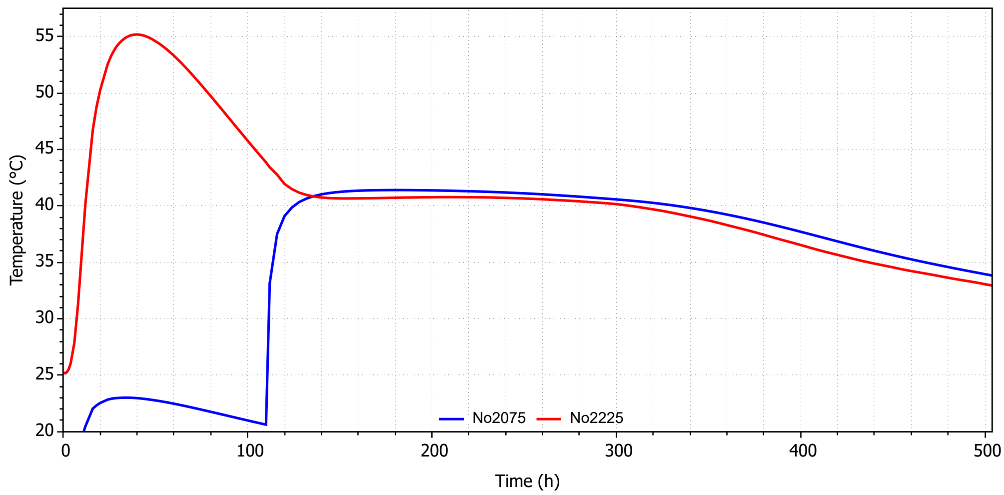

Figure 5.6: Simulation of the maximum temperature within the analysis

Furthermore, the cooling power for the pipe system has been determined. The maximum cooling power determined by the numerical simulation is around 96 W/m, resulting in the total power of 8.64 kW. This can be compared with the calculated power about 10.45 kW.

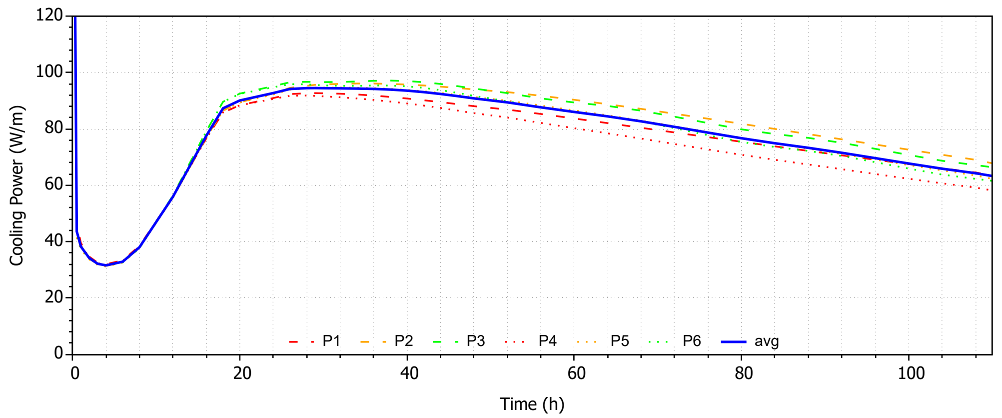

Figure 5.7: Cooling power of the system

The theoretical power is calculated based on the difference of the water temperature on input and output. If assuming the difference to be 5 °C and water flow about 0.5 l/s the total power can be determined according to:

$$P = \Delta T Q c \tag{5.1}$$

Please note, that the temperature of the water is assumed as constant for the whole pipe cooling system. Therefore, the cooling power for different locations does not differ so much. In reality, the cooling power along the length varies as the medium warms up resulting in higher difference between individual pipe's cooling power.

The visualisation of the thermal field for some of the analysis times are presented in the following Figure 5.9. The pilot block is cut at the mid-section.

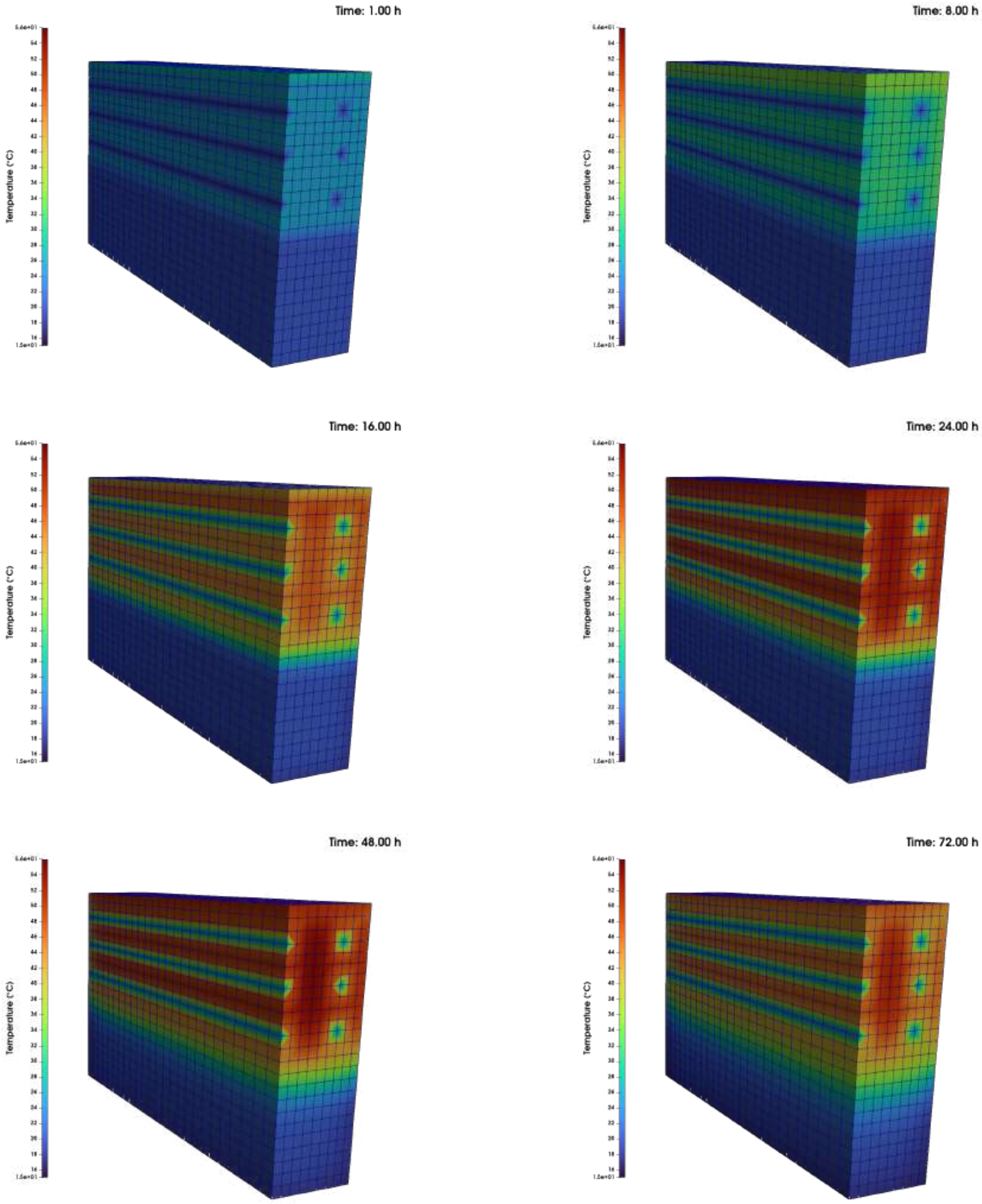

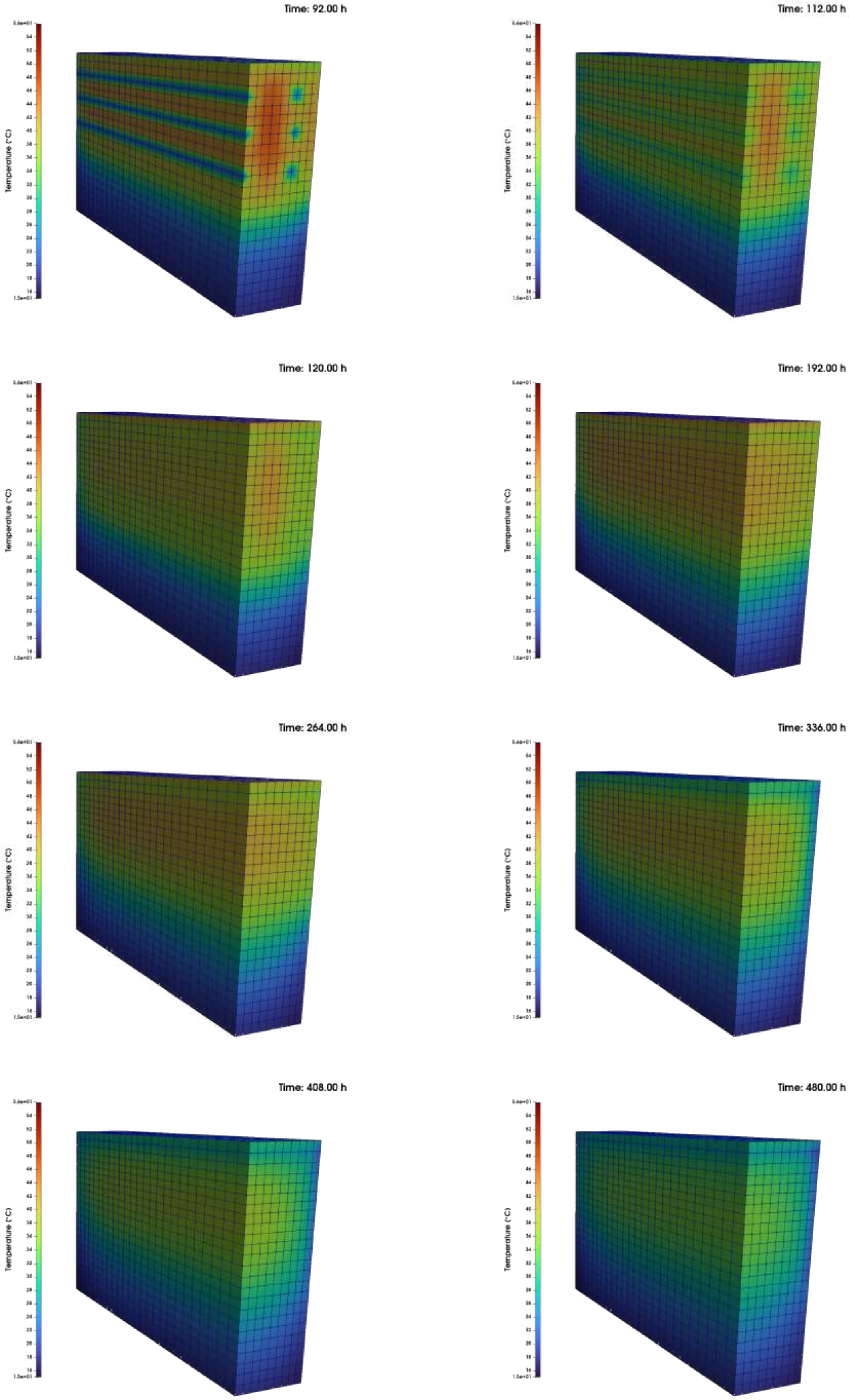

Figure 5.9: Thermal field results for several times of the analysis

5.3 Validation of mechanical model

To validate the reliability of the mechanical model, the numerical simulation results are compared with the field data, as illustrated in Figure 5.10. It should be noted that the data from strain gauge W1 are omitted from the analysis due to observed significant fluctuations. This suggests that the sensor may have been damaged during casting and measured data are unreliable. The remaining gauges, W2–W5, provide sufficiently reliable data for comparison. The results of measured strain by gauges are visualised as points while the simulation is represented with the full line, see Figure 5.10.

Right after casting, the readings from the installed gauges showed some fluctuations, but later became stable. For this reason, a reference time of 10 hours after the start of the analysis was chosen. At this point, the experimental strain values were set to zero. To ensure easy comparability of the results the simulation results are shifted to match this zero point.

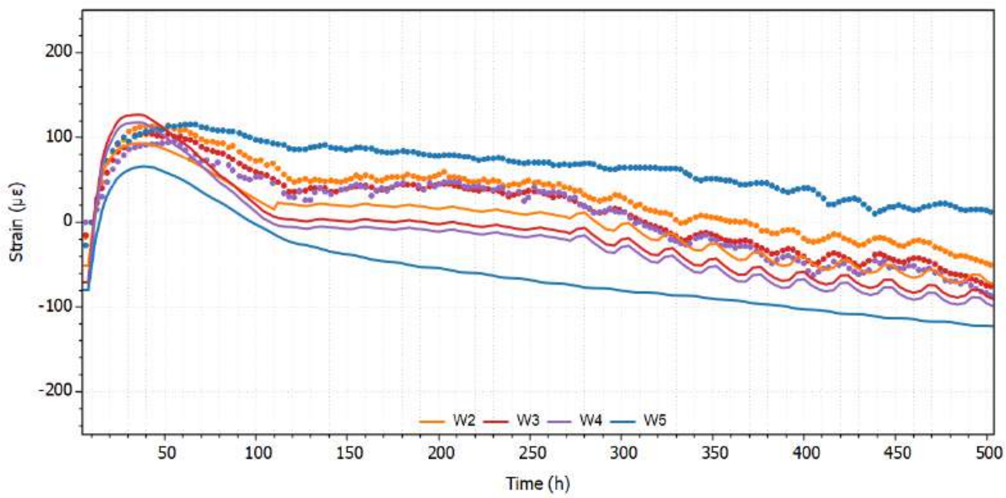

Figure 5.10: Validation of the mechanical model with experimental data (points - experiment, lines - model)

In general, the simulation results demonstrate a satisfactory level of agreement with the measured strains, apart from the exception for gauge W5. The numerical model successfully captures the overall evolution trend observed in the reality, including the timing and magnitude of the initial peak. However, discrepancies become evident during the cooling phase, particularly due to the model's tendency to overestimate the reduction in strain as the concrete block cools through embedded pipes. This results in lower predicted strain compared to the experimental measurements. Despite this limitation, the simulation provides a credible representation of the structural behaviour and supports the validity of the model.

5.4 Crack development

One of the most important outcomes, particularly from a practical perspective, is the evaluation of crack widths. In this specific application, no cracks were observed in the concrete block and the numerical simulation likewise does not predict any visible cracking. This result strongly reflects the quality of collaboration between the construction team and researchers. Achieving such a performance would not have been possible without thorough planning and preparation. However, it is important to note that the occurrence of cracking is highly dependent on the restraint conditions. When the base concrete is modelled as fully rigid, the simulation indicates the formation of cracks. A comparison of crack widths under the initially assumed conditions (left side) and modified rigid base layer (right side) is shown in the figures below. Also note that a scale factor of 1000 is used for visualising the crack width in the original scenario, in comparison the scale factor for second case is ten times lower.

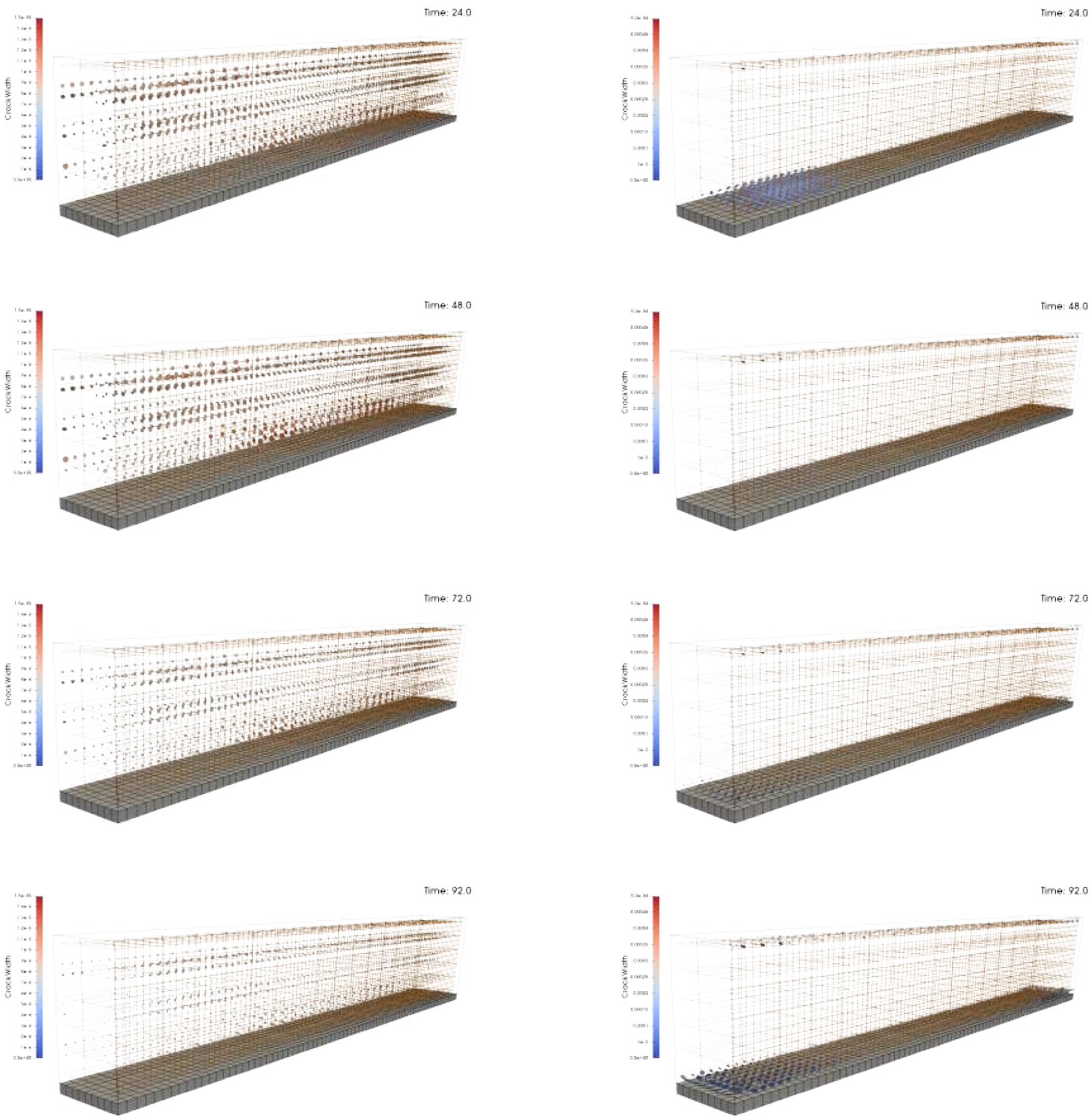

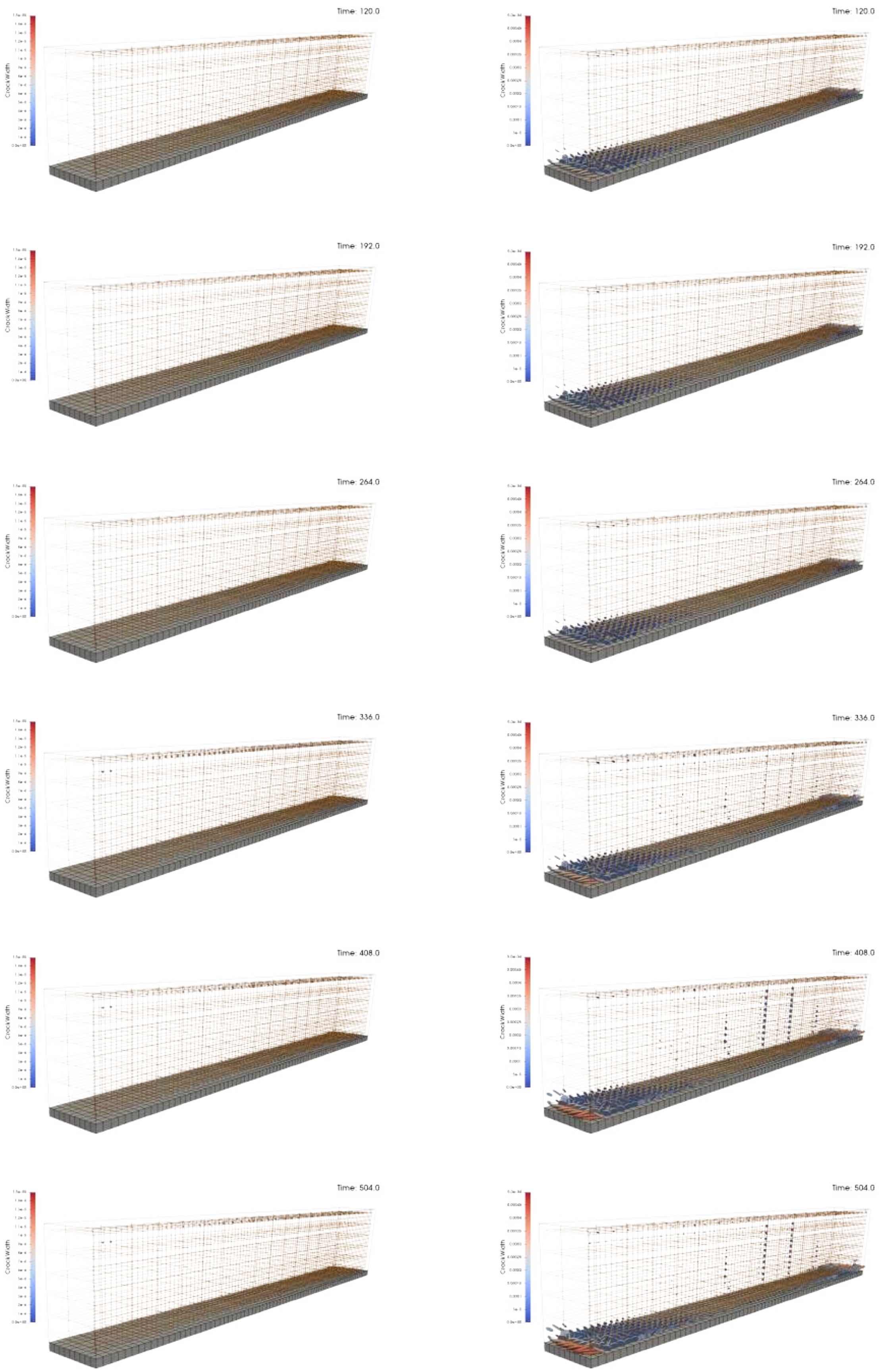

Figure 5.12: Crack development for several times of the analysis

Furthermore, the thermal analysis for the scenario with rigid base layer is extended to observe whether cracks develop in the middle section. It can be observed that around 768 hours, two cracks begin to form in the middle section, see Figure 5.13.

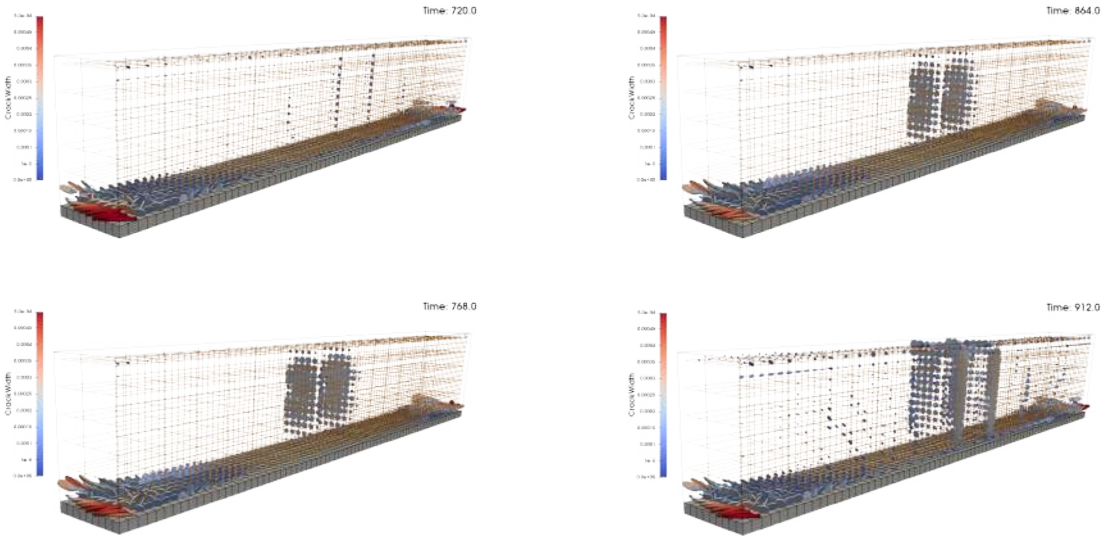

Figure 5.13: Crack development for rigid base concrete

Chapter 6

Conclusion

This work has presented complex thermal and mechanical behaviour of massive concrete structures, with a particular focus on the mitigation of early-age thermal cracking through the use of embedded pipe cooling system. Attention was also given to the theoretical background through a detailed literature review, which summarised existing knowledge on cement hydration, material models, cracking mechanism and various techniques to reduce risk of thermal cracking. By applying established material models within a numerical analysis and validating the results against field measurements from the Krounka polder pilot block, the work demonstrated the practical applicability of existing models.

All simulations were carried out using the open source finite element software OOFEM, which is a flexible and efficient tool for the coupled thermo-mechanical analysis. The thermal analysis is assumed as a transient heat conduction problem with employed affinity hydration model for concrete. It achieved excellent agreement with measured in situ temperature data. To reach this level of accuracy, it was necessary to carefully model a number of boundary conditions, including approximations of ambient temperature variation and the influence of solar radiation. This confirms that, when properly calibrated, the thermal analysis is highly effective in predicting the temperature evolution of early-age concrete.

The mechanical analysis focused on simulating strain and crack development resulting from thermal effects, as well as key time-dependent phenomena such as basic creep and autogenous shrinkage. The comparison with measured strains showed generally good correspondence. Moreover, no cracks were observed on the pilot block after casting, and this outcome was consistent with the results of the numerical simulation. However, a modified scenario of the simulation, which employed a rigid base layer, produced noticeably larger cracks. This is attributed to the excessive restraint imposed by the rigid layer, which not only restricts movement but also introduces unrealistic bending stiffness. As a consequence, overestimates the cracking risk. The modelling of boundary conditions, therefore, remains a key area where further refinement is necessary.

In conclusion, the numerical modelling is a reliable method for assessing early-age behaviour and cracking risk in massive concrete structures. Although thermal analysis is robust and accurate, mechanical model requires further improvement, particularly a refinement of the boundary conditions would be beneficial. One possibility for improvement is assuming boundary conditions resulting in statically determinate system. This allows for realistic bending flexibility and more accurate mechanical behaviour. Another possibility for future work is to incorporate moisture transport, resulting in a coupled thermo-hygro-mechanical model. This would enable modelling of drying shrinkage and creep. As a result, it can provide a more comprehensive and realistic representation of early-age concrete behaviour.

Bibliography

[1] ACI Committee 207. *ACI 207.4-20: Cooling and Insulating Systems for Mass Concrete*. American Concrete Institute, 2020.

[2] ACI Committee 301. *ACI 301-20: Specification for Concrete Construction*. American Concrete Institute, 2020.

[3] T. Ahmed, E. Burley, S. Rigden, and A. I. Abu-Tair. The effect of alkali reactivity on the mechanical properties of concrete. *Construction and Building Materials*, 17(2):123–144, 12 2002.

[4] F. Al-Neshawy. *Computerised prediction of the deterioration of concrete building facades caused by moisture and changes in temperature*. PhD thesis, Aalto University, School of Engineering, 2013.

[5] H. D. Baehr and K. Stephan. *Heat and Mass Transfer*. Springer, 2006.

[6] Z. P. Bažant and S. Baweja. Justification and refinements of model B3 for concrete creep and shrinkage 1. statistics and sensitivity. *Matériaux et Constructions*, 28(7):415–430, 8 1995.

[7] Z. P. Bažant, A. B. Hauggaard, S. Baweja, and F.-J. Ulm. Microprestress-Solidification Theory for Concrete Creep. I: Aging and drying Effects. *Journal of Engineering Mechanics*, 123(11):1188–1194, 11 1997.

[8] Z. P. Bažant and B. H. Oh. Crack band theory for fracture of concrete. *Matériaux et Constructions*, 16(3):155–177, 5 1983.

[9] Z. Bittnar and J. Šejnoha. *Numerické metody mechaniky 2 (Czech) [Numerical methods of mechanics 2]*. Vydavatelství ČVUT, 1992.

[10] Z. Bofang. *Thermal Stresses and Temperature Control of Mass Concrete*. Elsevier Inc., 2014.

[11] R. Carrazedo, R. A. K. Sanches, L. A. De Lacerda, and P. L. Divino. Concrete expansion induced by Alkali–Silica reaction in a small arch dam. *International Journal of Civil Engineering*, 16(3):289–297, 1 2017.

[12] M. Cervera, J. Oliver, and T. Prato. Thermo-chemo-mechanical model for concrete. i: Hydration and aging. *Journal of Engineering Mechanics ASCE*, 125(9):1018–1027, 1999.

[13] R. Courant. Variational methods for the solution of problems of equilibrium and vibrations. *Bulletin of the American Mathematical Society*, 49(1):1–23, 1 1943.

[14] EN 1992-1-1. *Eurocode 2: Design of concrete structures - Part 1-1: General rules and rules for buildings*. European Committee for Standardization, 2004.

[15] Fib. *Model Code for Concrete Structures 2010*. Federation Internationale Du Beton, 10 2013.

[16] P. Havlásek. *Creep and Shrinkage of Concrete Subjected to Variable Environmental Conditions*. PhD thesis, Czech Technical University in Prague, 2014.

[17] JCI. *Guidelines for Control of Cracking of Mass Concrete*. Japan Concrete Institute, 2016.

[18] M. Jirásek and P. Havlásek. Microprestress–solidification theory of concrete creep: Reformulation and improvement. *Cement and Concrete Research*, 60:51–62, 4 2014.

[19] W. Kurdowski. *Cement and Concrete Chemistry*. Springer Science + Business Media, 2014.

[20] M. Macho. *Modelování vodního chlazení masivních betonových konstrukcí (Czech) [Modeling of water cooling in massive concrete structures]*. CTU in Prague, Faculty of Civil Engineering, 2023.

[21] R. Malm. *Guideline for FE analyses of concrete dams, Report 2016:270*. Energiforsk AB, 2016.

[22] H. Mihashi and J. P. de B. Leite. State-of-the-art report on control of cracking in early age concrete. *Journal of Advanced Concrete Technology*, 2, 6 2004.

[23] Naše Martinice, webový zpravodaj. Začala stavba hráze protipovodňového poldru Kutřín za půl miliardy (Czech) [Construction of flood-prevetning polder Kutřín have begun with estimated cost of half billion]. *Naše Martinice, zapsaný spolek*, 2021.

[24] B. Patzák. OOFEM - an object-oriented simulation tool for advanced modeling of materials and structures. *Acta Polytechnica*, 52(6):59–66, 2012.

[25] B. Patzák. *OOFEM - Element Library Manual*. CTU in Prague, Faculty of Civil Engineering, 2018.

[26] B. Patzák. *OOFEM - Material Model Library Manual*. CTU in Prague, Faculty of Civil Engineering, 2019.

[27] B. Patzák. *OOFEM - Input Manual*. CTU in Prague, Faculty of Civil Engineering, 2021.

[28] Povodí Labe, státní podnik. Příprava výstavby poldru Krounka-Kutřín (Czech) [Construction preparation for polder Krounka-Kutřín]. not published.

[29] Z. Qu, Y. Zhang, Z. Liu, R. Si, and J. Wu. A Review on Early-age cracking of Concrete: Causes and Control. *Case Studies in Construction Materials*, 21, 2024.

[30] P. Reiterman, V. Davidová, T. David, and V. Šmilauer. Návrh a relizace vodního chlazení na štvanické lávce (Czech) [Design and Application of Water Cooling of Fresh Concrete on the Štvanice Footbridge]. *Beton*, (3):12–15, 2023.

[31] J. Ruiz, A. Schindler, R. Rasmussen, P. Kim, and G. Chang. *Concrete temperature modeling and strength prediction using maturity concepts in the FHWA HIPERPAV software*. 7th international conference on concrete pavements, Orlando (FL), 2001.

[32] SCIA Engineer. *Help page for SCIA 19*.

[33] R. M. Singh and A. Bouazza. Thermal conductivity of geosynthetics. *Geotextiles and Geomembranes*, 39:1–8, 2013.

[34] H. Taylor. *Cement Chemistry*. Academic Press, New York, 1990.

[35] M. J. Turner, R. W. Clough, H. C. Martin, and L. J. Topp. Stiffness and deflection analysis of complex structures. *Journal of the aeronautical sciences*, 23(9):805–823, 9 1956.

[36] K. Van Breugel. Artificial cooling of hardening concrete. *Delft University of Technology, Civil Engineering and Geosciences*, 1980.

[37] K. Van Breugel. Prediction of temperature development in hardening concrete. Prevention of thermal cracking in concrete at early stages. Report 15. *R. Springenschmid, EFN SPON*, 1998.

[38] K. Wallin, M. Emborg, and J. E. Jonasson. Värme ett aternativ till kyla (swedish) [warm as alternative to cooling]. *Luleå Tekniska Universitetet*, 1997.

[39] V. Červenka, L. Jendele, and J. Červenka. *ATENA Program Documentation - Part 1 Theory*. Červenka Consulting, 2016.

[40] Šindlar s.r.o., HG partner s.r.o. et al. Zadávací dokumentace - Projektová dokumentace (Czech) [Tender documentation – Project documentation]. Available online: `https://zakazky.eagri.cz/contract_display_14368.html`.

[41] V. Šmilauer and P. Reiterman. Měření teplot a deformací na zkušební lamele polderu Krounka, Kutřín (Czech) [Temperature and deformation measurument of polder Krounka pilot block]. not published.

[42] V. Šmilauer, P. Reiterman, P. Havlásek, and P. Huňka. Předběžný návrh betonů a postupu výstavby návodního líce polderu Kutřín na řece Krounka (Czech) Preliminary design of concrte and construction stages of upstream face of polder Kutřín on the Krounka stream. *BETON-technologie, konstrukce, sanace*, 20(6):44–49, 2020.

[43] V. Šmilauer, J. L. Vítek, B. Patzák, and Z. Bittnar. Optimalizace chlazení oblouku oparenského mostu (Czech) [Cooling Optimization in Oparno Bridge's Arch]. *Beton TKS*, 11(4):62–65, 2011.